

PIONIC ^{16}O - ^{18}O ISOTOPE EFFECTS

by

CHRISTINE IRENE SAYRE

B.Sc., University of Toronto, 1977

A THESIS SUBMITTED IN PARTIAL FULFILLMENT
OF THE REQUIREMENTS FOR THE DEGREE OF

MASTER OF SCIENCE

in the Department

of

Physics

ACCEPTED
FACULTY OF GRADUATE STUDIES


DATE


Sept 2, 83
A/DEAN

We accept this thesis as conforming
to the required standard


Dr. G.A. Beer


Dr. J. Muzio


Dr. A. Olin


Dr. F. Robinson

© CHRISTINE IRENE SAYRE, 1983

UNIVERSITY OF VICTORIA

June 1983

All rights reserved. This thesis may not be reproduced in
whole or in part, by mimeograph or other means, without
permission of the author.

QC 793.5
M428528

Supervisor: Professor George A. Beer

ABSTRACT

The pionic 2p-1s transition was observed in the isotope pair $^{16,18}\text{O}$. The 2p-1s X-ray energies and Lorentzian widths were measured, and the hadronic and isotope shifts were calculated. The results were:

	E (keV)	ϵ (keV)	Γ (keV)
^{16}O	160.286 (.090)	-15.13 (.13)	7.32 (.30)
^{18}O	155.792 (.160)	-19.63 (.20)	5.97 (.59)
Isotope Effect			
($^{18}\text{O} - ^{16}\text{O}$)		-4.50 (.24)	-1.35 (.66)

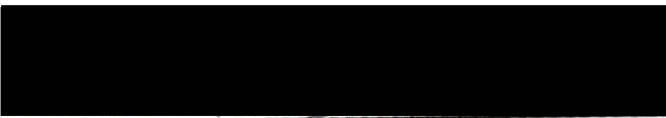
Comparison of the results with other experiments and theory shows good agreement for the isotope shifts and Lorentzian widths, but shows a systematic discrepancy between the present transition energies and other recent results. The discrepancy may be due to the use of different lineshape fitting functions in the two analyses. The experimental spectra also yielded measurements of the pionic 3d-2p

X-ray energies and Lorentzian widths, and the muonic $np-1s$ X-ray energies, up to $n=5$. The results were in agreement with other experiments.

Examiners:



Dr. G.A. Beer



Dr. J. Muzio



Dr. A. Olin



Dr. F. Robinson

CONTENTS

ABSTRACT.....	ii
TABLE OF CONTENTS.....	iv
LIST OF TABLES.....	vii
LIST OF FIGURES.....	ix
ACKNOWLEDGEMENTS.....	x
DEDICATION.....	xi
<u>Chapter</u>	<u>page</u>
I. INTRODUCTION.....	1
Pionic Atoms.....	1
Purpose and Scope of This Experiment.....	6
II. THEORETICAL TREATMENT OF PIONIC ATOMS.....	8
Introduction.....	8
The Optical Model Potential: a Multiple Scattering Approach.....	9
Free Pion-Nucleus Scattering.....	9
The Pion-Nucleus Potential.....	13
The Lorentz-Lorenz Effect.....	20
Pion Absorption and Nuclear Medium Effects.....	25
The $\pi^{16, 18}\text{O}$ Isotope Pair.....	29
Pionic Atom Calculations: the Program PIATOM.....	30
III. EXPERIMENTAL TECHNIQUE.....	32
Introduction.....	32
The Stopped Pion Channel.....	35

The Scintillation Telescope and Event Definitions.....	40
The Oxygen Targets.....	42
Calibration Sources.....	45
The Detector.....	45
The Circuit Logic and Data Acquisition System.....	47
Scintillator Telescope.....	47
Detector Signal Processing.....	49
Event Definition.....	50
Data Acquisition.....	51
IV. ANALYSIS OF THE DATA.....	54
Introduction.....	54
Data Acquisition.....	55
The Peak Fitting Program.....	56
The Detector Response Function.....	59
The Energy Calibration.....	65
Analysis of the Pionic ^{18}O 2p-1s X-ray Line.....	66
Analysis of the Pionic ^{16}O 2p-1s X-ray Line.....	74
Analysis of the Pionic $^{16},^{18}\text{O}$ 3d-2p X-ray Lines.....	78
Analysis of the Muonic $^{16},^{18}\text{O}$ X-ray Lines.....	82
V. DISCUSSION OF RESULTS AND CONCLUSIONS.....	86
Theoretical Predictions.....	86
Comparison of Results with Other Experiments and Theory.....	92
Conclusions and Recommendations.....	96

REFERENCES.....	98
-----------------	----

<u>Appendix</u>	<u>page</u>
-----------------	-------------

A. PARTIAL WAVE ANALYSIS OF PION-NUCLEON SCATTERING.....	102
--	-----

B. CALCULATION OF DEGRADER THICKNESS NECESSARY TO STOP PIONS IN THE OXYGEN TARGETS.....	107
--	-----

LIST OF TABLES

<u>Table</u>	<u>Page</u>
I. Negative Beam Particle Fluxes at F2.....	40
II. Estimated Amount of ^{16}O Present during Data Acquisition with the ^{18}O Target.....	44
III. Peaks Used to Determine the Detector Energy Resolution.....	61
IV. ^{75}Se Gamma Ray Peaks Used to Determine the Detector Efficiency Function.....	64
V. Typical Best Fit Tailing Parameters.....	65
VI. Peaks Used to Determine the Energy Calibration.....	68
VII. Peaks in the Fitting Window of the $\pi^{18}\text{O}$ 2p-1s X-ray.....	71
VIII. Peaks in the Fitting Window of the $\pi^{16}\text{O}$ 2p-1s X-ray.....	76
IX. Measured Energies, Hadronic Shifts and Widths of the $\pi^{16,18}\text{O}$ 2p-1s X-rays.....	77
X. Contributions to the Uncertainties in the Measured Energies and Widths of the $\pi^{16,18}\text{O}$ 2p-1s X-rays.....	77
XI. Comparison of Experimental Energies of the $\mu^{16}\text{O}$ and $\mu^{18}\text{O}$ np-1s X-rays with Recent Experimental Results.....	85

XII.	Comparison of the Measured Energies, Hadronic Shifts and Widths of the $\pi^{16,18}\text{O}$ 2p-1s X-rays with Other Experiments and Theory.....	89
XIII.	Pion-Nucleus Optical Potential Parameters Used in the Present Analysis.....	90
XIV.	Charge and Matter Distributions Used in the Theoretical Calculations of Energies and Linewidths.....	92
XV.	Comparison of Isotope Effects with Other Experiments and Theory.....	95

LIST OF FIGURES

<u>Figure</u>	<u>Page</u>
1. The M9 Channel.....	33
2. The Experimental Apparatus in the M9 Area.....	34
3. A Typical Time-of-Flight Spectrum.....	37
4. Range Curve in ^{18}O	39
5. The Oxygen Target Holder.....	39
6. The Circuit Logic.....	48
7. Detector Energy Resolution vs X-ray Energy.....	60
8. Detector Efficiency vs X-ray Energy.....	63
9. The Energy Calibration Curve.....	67
10. The $\pi^{18}\text{O}$ 2p-1s Fitting Window.....	70
11. The $\pi^{16}\text{O}$ 2p-1s Fitting Window.....	75
12. The $\pi^{18}\text{O}$ 3d-2p Fitting Window.....	80
13. The $\pi^{16}\text{O}$ 3d-2p Fitting Window.....	81
14. Comparison of the $\pi^{18}\text{O}$ 2p-1s X-ray Energy, Hadronic Shift and Width with Other Experiments and Theory.....	87
15. Comparison of the $\pi^{16}\text{O}$ 2p-1s X-ray Energy, Hadronic Shift and Width with Other Experiments and Theory.....	88

ACKNOWLEDGEMENTS

I would like to express my gratitude to the many people who helped to make this thesis possible. I would like to thank Dr. Michael Adam for his help with the mass spectroscopy tests of target materials, and Bruce Barnett and Bill Gyles for very useful discussions of target isotopic purity. I would like to thank Dr. Paul Poffenberger for his assistance in making the theoretical calculations. My special thanks go to the University of Victoria mesic X-ray group for their many hours of hard work in carrying out the measurements discussed in this thesis.

I would especially like to thank Dr. Arthur Olin for many interesting and fruitful discussions. My final thanks go to my supervisor, Dr. George Beer, for his help, encouragement and special efforts throughout this project.

DEDICATION

To the memory of the late

Professor R. Michael Pearce

CHAPTER 1

INTRODUCTION

1.1 Pionic Atoms

A negative pion passing through matter is slowed down by electromagnetic interactions with nearby atoms. When its kinetic energy is nearly zero, it may knock out one or more electrons from an atom and become bound electromagnetically to the nucleus in an electron-like orbit, forming a pionic atom. Not much is known about the capture process, but the cascade calculation is begun by assuming that the pion starts in an orbit just inside the electron 1s orbit, with the Bohr radii of the two orbits approximately equal (Backenstoss 1970)

$$r_e = \frac{1}{m_e Z \alpha} \approx r_\pi = \frac{n^2}{M_\pi Z \alpha} \quad (1.1)$$

$$\therefore n \cong \left(\frac{M_\pi}{m_e} \right)^{1/2} \cong 16, \quad (1.2)$$

where r_e and r_π are the Bohr radii of the electron and the pion, m_e and m_π are the reduced masses of the electron and the pion with respect to the nucleus, and n is the principal quantum number of the highest pion orbit.

The pion cascades down to lower levels, with Auger processes

dominating the higher n transitions and X-ray transitions dominating the lower ones. In Auger processes, $\Delta\ell=+1$ and large Δn are favoured, so these transitions tend mainly to populate lower circular orbits, for which $\Delta n=+1$. Once in a circular orbit, the pion can only make transitions to other circular orbits, thus the lower part of the pionic cascade is dominated by these so-called circular X-rays.

The highest pion orbit assumed in the cascade calculation is inside the electron cloud, where the interaction between the pion and the atomic electrons is small. Thus the pionic atom, in its cascade to lower levels, can be considered to be a hydrogen-like atom with nuclear charge $+Ze$, with a small correction for electron screening of the nuclear charge.

The motion of the bound pion is described by the Klein-Gordon equation

$$\{h^2 \nabla^2 + \frac{1}{c^2} [(E - V_e)^2 - \mu^2 c^4]\} \psi = \frac{2\mu}{h^2} V_N \psi \quad (1.3)$$

where E is the pion binding energy, including the pion rest mass; μ is the reduced mass of the pion-nucleus system; V_c is the total electromagnetic potential, including the finite extent of the nuclear charge, vacuum polarization, electron screening and any other desired electromagnetic corrections; V_N is the complex potential describing the strong pion-nuclear interaction; and ψ is the wavefunction of the bound pion.

The strong interaction between the pion and the nucleus shifts the

energy levels of the pionic atom away from purely electromagnetic values. The magnitude of the shift depends upon the amount of overlap between the pionic and nuclear wavefunctions, hence lower orbits and higher atomic numbers give larger shifts (Ericson and Ericson, 1966). As an example, the shift ϵ_{1s} of the $1s$ level in $\pi^{16}\text{O}$ is about 10% of the $2p-1s$ transition energy.

There is, however, a limit to the observed energy shifts. Since the pion is a boson, it can be absorbed by the nucleons in the nucleus, i.e., the process $N+\pi \rightarrow N$ is possible. Conservation of energy and momentum makes absorption on a single nucleon unlikely. If the pion has zero momentum, the absorbing nucleon leaves the nucleus with kinetic energy $p_0^2/2M = \mu - \epsilon$, where ϵ is the nucleon binding energy and μ is the reduced pion mass. This corresponds to a momentum $p_0 \cong \sqrt{2\mu M} \cong 500 \text{ MeV}/c$, but since the Fermi momentum of nucleons in the nucleus is only about $250 \text{ MeV}/c$, the probability of a bound nucleon having such a high momentum is very small. Absorption on a pair of nucleons is much more likely, with the two nucleons sharing the energy equivalent of the pion's rest mass roughly equally, so that $p_0^2/2m \cong \mu/2$; then $p_0 \cong \sqrt{\mu M} \cong 360 \text{ MeV}/c$. This is the principal absorption mechanism, although in a few experiments on light nuclei absorption on alpha clusters is also considered important (Hüfner 1975).

Direct nuclear absorption of the pion from a given state shortens the lifetime of that state, thus broadening the electromagnetic level width due to radiative and Auger transitions. For example, the $1s$ level

level width in pionic ^{16}O is about 5% of the $2p-1s$ transition energy. From a first order perturbation theory argument, the widths increase with Z roughly as $Z^{4/3}(2\ell+3)$ (Ericson 1970), so that for a given ℓ the absorption increases dramatically with Z until at some point the X-ray transition to that state is no longer observable. For example, X-ray transitions to the $1s$ state ($2p-1s, 3p-1s, \dots$) are observed only for $Z \leq 11$, to the $2p$ state ($3d-2p, \dots$) only for $Z \leq 30$, and to the $3d$ state ($4f-3d, \dots$) only for $Z \leq 59$ (Ericson 1970).

Pions decay to muons; the mean lifetime of a pion is 2.6×10^{-8} s (Particle Data Group 1978). Since the mean lifetime of pionic atoms is about 10^{-13} s (Backenstoss 1970), the number of pions decaying to muons in orbit is negligible. However, where pions are being stopped in target material to form pionic atoms, the decay of pions in the incoming pion beam and in the target itself results in the presence of muons in the target material and surroundings. Some of these muons will be stopped and will form muonic atoms by a capture process similar to that for pionic atoms. Since the muon does not interact strongly with the nucleus, the energy levels of the muonic atom are purely electromagnetic. The shifts due to finite size and vacuum polarization are the principal corrections to the point nuclear energies. The relative proportion of pionic and muonic X-rays observed in any given experiment is controlled by adjusting the ratio of pions to muons stopping in the target; this is done by tuning the pion channel, or by other experimental means.

In a typical pionic X-ray experiment, the energies and widths of the X-ray transitions are the principal quantities measured. The strong interaction shifts $\epsilon_{n\ell}$ and widths $\Gamma_{n\ell}$ are deduced from the transition shifts and widths using

$$\epsilon_{n\ell} = E_{n',\ell' \rightarrow n\ell} - E_{em} \quad (1.4)$$

$$\Gamma_{n\ell} = \Gamma_{n',\ell' \rightarrow n\ell} - \Gamma_{em}$$

where $E_{n',\ell' \rightarrow n\ell}$ and $\Gamma_{n',\ell' \rightarrow n\ell}$ are the energy and width of the transition $(n',\ell' \rightarrow n,\ell)$, and E_{em} and Γ_{em} are the purely electromagnetic values for the same transition. The strong interaction shift and width of the upper level (n',ℓ') in the transition $(n',\ell' \rightarrow n,\ell)$ can be neglected. In practice E_{em} is calculated using a computer code (e.g., Krell 1977) to solve numerically the Klein-Gordon equation

$$\left\{ \nabla^2 + \frac{1}{\hbar^2 c^2} [(E - V_c)^2 - \mu^2 c^4] \right\} \psi = 0 \quad (1.5)$$

for the energy eigenvalues. The potential V_c contains the effects of the finite extent of the nuclear charge and the first order vacuum polarization, but higher orders of vacuum polarization and electron screening are not included since they are negligible for the lower transitions of interest in pionic X-ray experiments. Thus, deduction of the strong interaction shifts assumes a good knowledge of electromagnetic effects, including nuclear charge distributions. In most cases, the charge distributions are well-known from muonic atom

and electron scattering experiments.

The strong interaction shifts and level widths are used to determine parameters in the complex potential describing the strong pion-nuclear interaction. Most commonly, an optical potential is used, as described more fully in Chapter II. The nucleus is treated as a collection of fixed scatterers, with the bound pion considered to scatter off the individual nucleons at zero energy. This scattering is averaged over the continuous nuclear matter distribution $\rho(r)$, with the granularity in the nuclear structure being taken into account chiefly through the Lorentz-Lorenz term (Sect. 2.4). The π -N scattering lengths appear explicitly in the optical potential. Thus results of pionic X-ray experiments can be related to low energy elastic π -N and π -nuclear scattering experiments, although the elementary π -N scattering amplitudes must be corrected for nuclear medium effects (Ericson and Ericson 1966). The level widths of pionic X-rays are a direct measure of the pion absorption term in the potential, which is difficult to measure in scattering experiments.

1.2 Purpose and scope of this experiment

In this experiment, pionic X-ray spectra of the two isotopes ^{16}O and ^{18}O were obtained. Broadened $2p-1s$ X-rays were observed in the spectra of each isotope, and the transition energies E_{2p-1s} and level widths Γ_{1s} were measured. The electromagnetic transition energies were calculated as described above, using the computer code PIATOM (Krell 1977); they were then subtracted from E_{2p-1s} to

give the strong interaction shifts ϵ_{1s} . The spectra also contained muonic X-ray lines of sufficient intensity that the muonic np-1s ($n \leq 5$) transition energies were measured in both oxygen isotopes.

The isotope pair $^{16,18}\text{O}$ is particularly interesting since both proton distributions are well-known to be nearly equal from recent electron elastic scattering experiments (Miska 1979), so that the isotope shifts

$$\begin{aligned}\Delta\epsilon_{1s} &= \epsilon_{1s}(^{18}\text{O}) - \epsilon_{1s}(^{16}\text{O}) \\ \Delta\Gamma_{1s} &= \Gamma_{1s}(^{18}\text{O}) - \Gamma_{1s}(^{16}\text{O})\end{aligned}\quad (1.6)$$

each reflect the effects of adding two neutrons to the doubly magic nucleus ^{16}O . If an isovector degree of freedom is added to the s-wave absorption part of the optical potential, as in the recent work by Powers et al. (Powers 1980), then the ^{18}O level width Γ_{1s} becomes particularly interesting, especially since ^{18}O is one of two isospin 1 nuclei with Z low enough that the 2p-1s transition is observable.

CHAPTER 2

THEORETICAL TREATMENT OF PIONIC ATOMS

2.1 Introduction

The motion of a pion in orbit around an atomic nucleus is described by the Klein-Gordon equation (1.3), which includes two potential terms: V_c is the electromagnetic potential due to the distributed nuclear charge $+Ze$; V_N is the strong interaction potential due to all of the nucleons in the nucleus. Most often, the potential V_N is derived using an optical model, in which the strong interaction of a pion with a nucleus is treated in analogy with the scattering of light off the atoms in dense media. The equations for the multiple scattering of the pion off the nucleons in the nucleus, in a partial wave expansion (Section 2.2.1), give rise to an optical potential with a large dipole scattering term (Section 2.2.2). Using this potential in first order perturbation theory, energy level shifts in pionic atoms are related to the π -N scattering lengths (Section 2.2.2). When short-range nucleon-nucleon correlations are included, the dipole scattering produces a Lorentz-Lorenz effect (Section 2.2.3) analogous to the change in refractive index in classical media when atom-atom correlations are taken into account.

An imaginary part is then added to the optical potential to

account for pion absorption, which is not a multiple scattering effect (Section 2.3). Corrections for nuclear medium effects are discussed in the same section. The significance of the experimental 1s energies, level shifts and widths of the pionic $^{16,18}\text{O}$ isotope pair is discussed (Section 2.4), and the procedure used to make theoretical calculations of these quantities is briefly described (Section 2.5).

2.2 The optical model potential: a multiple scattering approach

2.2.1 Free pion-nucleon scattering

We begin by considering elastic pion-nucleon scattering, taking into account only spin and orbital angular momentum states, but not isospin yet. Following the development of Williams (1971), the incoming wave may be taken as $\Psi = e^{ikz}$, and the outgoing wave as

$$\psi_{\text{out}} = e^{ikz} + f(E, \theta) \frac{e^{ikr}}{r} \quad (2.1)$$

where e^{ikz} is the undisturbed part of the incoming wave, and e^{ikr}/r is the scattered wave, with amplitude $f(E, \theta)$; the dependence of the scattering amplitude on the energy of the incoming particle is explicitly included. The total probability for the scattered wave to be detected at a given angle θ is the differential cross-section, $d\sigma/d\Omega$, which is related to the scattering amplitude by

$$\frac{d\sigma}{d\Omega} = |f(E, \theta)|^2. \quad (2.2)$$

Differential cross-sections are measured directly in scattering experiments, and the scattering amplitudes are obtained from analysis of the results. Following the arguments in Appendix A, the scattering

amplitude may be expanded in partial waves to give

$$f(E, \theta) = \sum_{\ell=0}^{\infty} \left\{ [f_{\ell-} + (\ell+1)f_{\ell+}] P_{\ell}(\cos\theta) \right\} f - i\vec{\sigma} \cdot \frac{\vec{k} \times \vec{k}'}{|\vec{k} \times \vec{k}'|} \sum_{\ell=0}^{\infty} \left\{ [f_{\ell-} - f_{\ell+}] P_{\ell}^1(\cos\theta) \right\}, \quad (2.3)$$

where the $f_{\ell\pm}$ are the partial wave amplitudes for the scattering of the ℓ^{th} partial wave in the states $j = \ell \pm 1/2$ and where $\vec{k} = \vec{k}'/|\vec{k}'|$, with \vec{k} and \vec{k}' the incoming and outgoing pion momenta, respectively. Restricting the expansion to s- and p-waves only (this will be justified below),

$$f(E, \theta) \cong f_{s1/2} + (f_{p1/2} + 2f_{p3/2}) \cos\theta - i\vec{\sigma} \cdot \frac{\vec{k} \times \vec{k}'}{|\vec{k} \times \vec{k}'|} (f_{p1/2} - f_{p3/2}) \sin\theta. \quad (2.4)$$

The scattering lengths and volumes are defined by

$$\lim_{k \rightarrow 0} \frac{f_{\ell j}}{k^{2\ell}} \equiv a_{\ell j}. \quad (2.5)$$

Since the bound pion can be considered to scatter off the nucleus at the zero incident energy threshold, the partial wave amplitudes $f_{\ell j}$ can be written in terms of the scattering lengths, i.e.,

$$f_{\ell j} \rightarrow a_{\ell j} k^{2\ell}, \text{ and then } f(E, \theta) \text{ can be written as } f(\theta), \text{ where} \\ f(\theta) = a_{s1/2} + (a_{p1/2} + 2a_{p3/2}) k^2 \cos\theta - i\vec{\sigma} \cdot \frac{\vec{k} \times \vec{k}'}{|\vec{k} \times \vec{k}'|} (a_{p1/2} - a_{p3/2}) k^2 \sin\theta \quad (2.6)$$

Since the scattering is elastic, and the nucleon scatterers considered

fixed, $|\vec{k}| = |\vec{k}'|$, so that

$$\begin{aligned} k^2 \cos \theta &= \vec{k} \cdot \vec{k}' \\ \sin \theta &= |\vec{k} \times \vec{k}'| \\ (\vec{k} \times \vec{k}')^2 &= \vec{k} \times \vec{k} \end{aligned} \quad (2.7)$$

Making these substitutions, (2.6) becomes

$$f(\theta) = a_{s1/2} + (a_{p1/2} + 2a_{p3/2}) \vec{k} \cdot \vec{k}' - i \vec{\sigma} \cdot \vec{k} \times \vec{k}' (a_{p1/2} - a_{p3/2}) \quad (2.8)$$

Now introducing the isospin decomposition, only two charge states, $T=1/2$ and $T=3/2$, where T is the total isospin, are available to the $|\pi N\rangle$ system. To create a projection operator for these two states, define \vec{t} = pion isospin, $\frac{\vec{\tau}}{2}$ = nucleon isospin, and take

$$\begin{aligned} \vec{T} &= \vec{t} + \frac{\vec{\tau}}{2} \\ \vec{T}^2 &= \vec{t}^2 + \left(\frac{\vec{\tau}}{2}\right)^2 + \vec{t} \cdot \vec{\tau} \\ \langle \vec{T} | \vec{t} \cdot \vec{\tau} | \vec{T} \rangle &= T(T+1) - t(t+1) - \frac{\tau(\tau+1)}{2} \\ &= T(T+1) - 2 - \frac{3}{4} \end{aligned} \quad (2.9)$$

Therefore define the projection operator for $T = \frac{3}{2}$ as $\frac{1}{3}(2 + \vec{t} \cdot \vec{\tau})$, where

$$\begin{aligned} \langle \vec{T} | \frac{1}{3}(2 + \vec{t} \cdot \vec{\tau}) | \vec{T} \rangle &= 1, \quad T = \frac{3}{2} \\ &= 0, \quad T = \frac{1}{2} \end{aligned} \quad (2.10)$$

and the projection operator for $T = \frac{1}{2}$ as $\frac{1}{3}(1 - \vec{t} \cdot \vec{\tau})$, where

$$\begin{aligned} \langle \vec{T} | \frac{1}{3}(1 - \vec{t} \cdot \vec{\tau}) | \vec{T} \rangle &= 0, \quad T = \frac{3}{2} \\ &= 1, \quad T = \frac{1}{2} \end{aligned} \quad (2.11)$$

Then introducing isospin explicitly into (2.8), and defining the s- and p-wave scattering lengths α_{2T} and α_{2T2J} ,

$$f(\Theta) = \frac{1}{3}(2+\vec{t} \cdot \vec{\tau})f_3 + \frac{1}{3}(1-\vec{t} \cdot \vec{\tau})f_1 \quad (2.12)$$

where $\langle \vec{T} | f(\Theta) | \vec{T} \rangle$ is the total pion-nucleus scattering amplitude, and $\langle \vec{T} | f_3 | \vec{T} \rangle$ and $\langle \vec{T} | f_1 | \vec{T} \rangle$ are the scattering amplitudes for $T = \frac{3}{2}$ and $T = \frac{1}{2}$ states, respectively, i.e.,

$$\begin{aligned} f_3 &= \alpha_3 + (\alpha_{31} + 2\alpha_{33})\vec{k} \cdot \vec{k}' - i\vec{\sigma} \cdot \vec{k} \times \vec{k}' (\alpha_{31} - \alpha_{33}) \\ f_1 &= \alpha_1 + (\alpha_{11} + 2\alpha_{13})\vec{k} \cdot \vec{k}' - i\vec{\sigma} \cdot \vec{k} \times \vec{k}' (\alpha_{11} - \alpha_{13}) \end{aligned} \quad (2.13)$$

so that

$$\begin{aligned} f(\Theta) &= \frac{1}{3}(2\alpha_3 + \alpha_1) + \frac{1}{3}(\alpha_3 - \alpha_1)\vec{t} \cdot \vec{\tau} \\ &+ \left[\frac{1}{3}(2\alpha_{31} + 4\alpha_{33} + \alpha_{11} + 2\alpha_{13}) + \frac{1}{3}(\alpha_{31} + 2\alpha_{33} - \alpha_{11} - 2\alpha_{13})\vec{t} \cdot \vec{\tau} \right] \vec{k} \cdot \vec{k}' \\ &- i\vec{\sigma} \cdot \vec{k} \times \vec{k}' \left[\frac{1}{3}(2\alpha_{31} - 2\alpha_{33} + \alpha_{11} - \alpha_{13}) + \frac{1}{3}(\alpha_{31} - \alpha_{33} - \alpha_{11} + \alpha_{13})\vec{t} \cdot \vec{\tau} \right]. \end{aligned} \quad (2.14)$$

This can be written more simply as

$$f(\Theta) = b_0 + b_1\vec{t} \cdot \vec{\tau} + [c_0 + c_1\vec{t} \cdot \vec{\tau}]\vec{k} \cdot \vec{k}' - i[d_0 + d_1\vec{t} \cdot \vec{\tau}]\vec{\sigma} \cdot \vec{k} \times \vec{k}' \quad (2.15)$$

where

$$\begin{aligned} b_0 &= \frac{1}{3}(2\alpha_3 + \alpha_1), \quad \text{the isoscalar s-wave parameter;} \\ b_1 &= \frac{1}{3}(\alpha_3 - \alpha_1), \quad \text{the isovector s-wave parameter;} \\ c_0 &= \frac{1}{3}(2\alpha_{31} + 4\alpha_{33} + \alpha_{11} + 2\alpha_{13}), \quad \text{the isoscalar p-wave parameter;} \\ c_1 &= \frac{1}{3}(\alpha_{31} + 2\alpha_{33} - \alpha_{11} - 2\alpha_{13}), \quad \text{the isovector p-wave parameter;} \\ d_0 &= \frac{1}{3}(2\alpha_{31} - 2\alpha_{33} + \alpha_{11} - \alpha_{13}), \quad \text{the isoscalar spin-dependent} \\ &\quad \text{p-wave parameter;} \\ d_1 &= \frac{1}{3}(\alpha_{31} - \alpha_{33} - \alpha_{11} + \alpha_{13}), \quad \text{the isovector spin-dependent} \\ &\quad \text{p-wave parameter.} \end{aligned} \quad (2.16)$$

The experimental values for these parameters, in the low energy limit for free π -nucleon scattering, are (Nagels 1979):

$$\begin{aligned}
b_0 &= (-0.013 \pm .003)m_\pi^{-1} & b_1 &= (-0.092 \pm .001)m_\pi^{-1} \\
c_0 &= (0.209 \pm .005)m_\pi^{-3} & c_1 &= (0.177 \pm .003)m_\pi^{-3} \\
d_0 &= (0.189 \pm .003)m_\pi^{-3} & d_1 &= (0.070 \pm .002)m_\pi^{-3}
\end{aligned} \tag{2.17}$$

Because b_0 is so small, the s-wave π^-n scattering length $(b_0 + b_1)$ is almost the same as the s-wave π^-p scattering length $(b_0 - b_1)$, except that their signs are opposite. The p-wave π^-p scattering length $(c_0 - c_1)$ is very small, so there is very little π^-p interaction in p-wave π^-N scattering.

To obtain a potential which gives the correct free π^-N scattering amplitude, a short-ranged pseudopotential $V(r)$ is introduced, and $f(\theta)$ is written, in the plane-wave Born approximation

$$f(\theta) = \frac{-m}{2\pi\hbar^2} \int e^{-i\vec{k}' \cdot \vec{r}} V(\vec{r}) e^{i\vec{k} \cdot \vec{r}} d\vec{r}. \tag{2.18}$$

Inverting this, and using (2.5), the potential for a pion scattering off a nucleon at \vec{r}_i is

$$\begin{aligned}
V(\vec{r}) &= \frac{-2\pi\hbar^2}{m\pi} \int f(\theta) e^{-i(\vec{k}-\vec{k}') \cdot \vec{r}} d^3(\vec{k}-\vec{k}') \\
&= \frac{-2\pi\hbar^2}{m\pi} \{ b_0 + b_1 \vec{t} \cdot \vec{\tau} + [c_0 + c_1 \vec{t} \cdot \vec{\tau}] \vec{k} \cdot \vec{k}' \\
&\quad - i[d_0 + d_1 \vec{t} \cdot \vec{\tau}] \vec{\sigma} \cdot \vec{k} \times \vec{k}' \} \delta(\vec{r} - \vec{r}_i).
\end{aligned} \tag{2.19}$$

2.2.2 The pion-nucleus potential

The scattering amplitude for a pion off a bound nucleon in the nucleus can be considered to be the same as the amplitude for free π^-N scattering, except for kinematical factors. In the impulse approximation, the π^-N scattering is considered to occur at zero range. At low pion energies, this approximation is expected to be good,

especially since the π^-N interaction has a short range (Ericson and Ericson 1966). The amplitude for the pion to scatter off the i^{th} nucleon, from (2.15), is then

$$f_i(\theta) = f(\theta) \delta(\vec{r} - \vec{r}_i). \quad (2.20)$$

This can be summed over all the nucleons in the nucleus, to give the pion-nucleus scattering amplitude

$$f_N(\theta) = \sum_{p,n} f_i(\theta) = f(\theta) \rho(\vec{r}) \quad (2.21)$$

where

$$\rho(\vec{r}) = \rho_n(\vec{r}) + \rho_p(\vec{r}).$$

This summation is done in the fixed scatterer, or frozen nucleus, approximation, by first taking all the nucleon positions as fixed, then averaging over the total nuclear wavefunction. Nuclear recoil effects are thus neglected. While this approximation is very poor in the region of the (3,3) resonance at 180 MeV, it is good in the limit of very low pion energies, which certainly applies to pionic atoms (Scheck 1975).

This brings up the question of off-shell effects. A theorem due to Bèg states that: If the fixed scatterer approximation holds, and the internucleon distances are greater than twice the range of the π^-N interaction, then the π^-N interaction regions never overlap, and only on-shell π^-N scattering contributes to the pion-nucleus scattering matrix (Hüfner 1975). This is because the pion traverses a force-free region between scatterings, and in this region the pion

wavefunction is on-shell, i.e., $|\vec{k}| = |\vec{k}'|$. In the impulse approximation, the assumed zero-range πN scattering potential is averaged over a homogeneous nuclear medium (2.21). In actual pion-nucleus scattering, repulsive nucleon-nucleon correlations are important; when they are taken into account (this is just the inclusion of the Lorentz-Lorenz effect in the potential, cf. Section 2.2.3), the condition of non-overlapping potentials is fulfilled, and off-shell effects are negligible (Scheck 1975). In the free πN scattering amplitude, the terms in $\vec{k} \cdot \vec{k}$ and $\vec{k} \times \vec{k}$ come from the assumption that $|\vec{k}| = |\vec{k}'|$. Since pion-nucleus scattering is almost entirely on-shell, these terms may be kept unmodified in the pion-nucleus optical potential.

The contributions of the spin-dependent terms in d_0 and d_1 to the total interaction have been estimated to be of order A^{-1} and A^{-2} , respectively (Ericson and Ericson 1966) and may be neglected (Backenstoss 1970). Using the identity

$$\vec{k} = -ie^{-i\vec{k}\cdot\vec{r}} \vec{\nabla}_e e^{i\vec{k}\cdot\vec{r}} \quad (2.22)$$

terms in $\vec{k} \cdot \vec{k}' \rho(\vec{r})$ are transformed to terms of the form $\vec{\nabla} \rho(\vec{r}) \cdot \vec{\nabla}$

(Backenstoss 1970). Simplifying terms in $\vec{t} \cdot \vec{t} \rho(\vec{r})$,

$$\begin{aligned} \vec{t} \cdot \vec{t} \rho(\vec{r}) &= (\vec{t} \cdot \vec{t}) [\rho_n(\vec{r}) + \rho_p(\vec{r})] \\ &= \rho_n(\vec{r}) - \rho_p(\vec{r}), \end{aligned} \quad (2.23)$$

since $\vec{t} \cdot \vec{t} = +1$ for neutrons, and -1 for protons. The pion-nucleus potential may then be obtained from $f_N(\theta)$ by a procedure analogous to

(2.18) and (2.19)

$$V_N(\vec{r}) = \frac{-2\pi\hbar^2}{\mu_\pi} p_1 \{ b_0 \rho(\vec{r}) + b_1 [\rho_n(\vec{r}) - \rho_p(\vec{r})] + \vec{\nabla} [c_0 \rho(\vec{r}) + c_1 (\rho_n(\vec{r}) - \rho_p(\vec{r}))] \cdot \vec{\nabla} \} \quad (2.24)$$

where $\mu_\pi = m_\pi (1 + \frac{m_\pi}{M})^{-1}$ is the reduced mass of the pion-nucleus system, and $p_1 = (1 + \frac{m_\pi}{m_n})$ transforms the coordinates from the pion-nucleon to the pion-nucleus centre of mass system.

Using this zero-range potential in a first-order perturbation approximation, the energy shift due to the pion-nucleus strong interaction can be related to the scattering lengths for the partial wave. Following the development of Ericson (1970), in a first-order perturbation expansion, using the Born approximation, the scattering amplitude is

$$f(\theta) = \frac{-2m_\pi}{4\pi} \int e^{-i\vec{k}' \cdot \vec{r}} V(\vec{r}) e^{i\vec{k} \cdot \vec{r}} d\vec{r} . \quad (2.25)$$

To project out the leading contribution of the ℓ^{th} partial wave,

$e^{i(\vec{k}' - \vec{k}) \cdot \vec{r}}$ was expanded in partial waves and integrated to obtain

$$f_\ell(\theta) = \frac{-2m_\pi}{4\pi} (2\ell+1) \left[\int j_\ell^2(kr) V(\vec{r}) d^3r \right] P_\ell(\cos\theta) \quad (2.26)$$

where $P_\ell(\cos\theta)$ is the ℓ^{th} Legendre polynomial, and $j_\ell(kr)$ is a spherical Bessel function, which can be approximated by

$$j_\ell(kr) \cong \frac{k^\ell r^\ell}{(2\ell+1)!!} \quad (2.27)$$

for $kr \ll 1$, which certainly holds for pionic atoms, where the incident

pion energy is zero. Using this approximation, (2.26) becomes

$$f_{\ell}(\Theta) = \frac{-2m\pi}{4\pi}(2\ell+1) \frac{k^{2\ell}}{[(2\ell+1)!!]^2} \left[\int r^{2\ell} V(r) d^3r \right] P_{\ell}(\cos\Theta) \quad (2.28)$$

From equation (A.5), the contribution of the ℓ^{th} partial wave to the total scattering amplitude $f(\Theta)$ is

$$f_{\ell}(\Theta) = (2\ell+1)a_{\ell} k^{2\ell} P_{\ell}(\cos\Theta) \quad (2.29)$$

where a_{ℓ} is the generalized scattering length for the ℓ^{th} partial wave. Comparing (2.28) and (2.29),

$$a_{\ell} = \frac{-2m\pi}{4\pi} \frac{1}{[(2\ell+1)!!]^2} \int r^{2\ell} V(r) d^3r \quad (2.30)$$

Now the energy shift, in a first-order perturbation expansion, is

$$\begin{aligned} \Delta E_{n\ell} &\cong \int V(\vec{r}) |\Psi_{n\ell}|^2 d\vec{r} \\ &= \int V(\vec{r}) |Y_{\ell m} \phi_{n\ell}|^2 d\vec{r} \\ &= \frac{1}{4\pi} \int V(r) \phi_{n\ell}^2 dr \\ &= A_{n\ell} r_B^{2\ell-3} \frac{1}{4\pi} \int r^{2\ell} V(r) dr \end{aligned} \quad (2.31)$$

where

$$r_B = \frac{1}{m_{\pi} Z\alpha}.$$

Here r_B is the Bohr radius for a pionic atom with nuclear charge $+Ze$,

$\Psi_{n\ell}$ is taken to be an unperturbed hydrogenic wavefunction, and

$A_{n\ell}$ contains numerical factors in n and ℓ . Eliminating the common

factor $\int r^{2\ell} V(r) dr$, and taking the ratio of $\Delta E_{n\ell}$ to the

Klein-Gordon electromagnetic energy $E_{n\ell}$, where

$$E_{n\ell} = \frac{-m_{\pi}(Z\alpha)^2}{2n^2} \left\{ 1 + \frac{(Z\alpha)^2}{n^2} \left(\frac{n}{\ell+\frac{1}{2}} - \frac{3}{4} \right) - \dots \right\} \quad (2.32)$$

the relationship between $E_{n\ell}$ (or $\epsilon_{n\ell}$) and $A_{n\ell}$ is (Ericson 1970)

$$\frac{\epsilon_{n\ell}}{E_{n\ell}} = -\frac{4}{n} \frac{a_{\ell}}{(\ell!)^2} \frac{1}{r_B^{2\ell+1}} \left(1 - \frac{1}{n}\right) \dots \left(1 - \frac{\ell^2}{n}\right) \quad (2.33)$$

Now the neglect of higher partial waves ($\ell > 2$) in the optical potential may be examined. If a pion is in a state with angular momentum ℓ with respect to the nucleus, it may be assumed, in a first approximation, that it also has the same angular momentum with respect to the individual nucleons. The total scattering length can then be taken as the coherent sum of π^-N scattering lengths

$$a_{\ell} = Z a_{\pi^-p}^{\ell} + N a_{\pi^-n}^{\ell} . \quad (2.34)$$

Using experimental values of the π^-N scattering lengths, the coherent sums $a_{n\ell}$, for $\ell=0,1,2,3$, were obtained and used to predict values of the ratios $\epsilon_{n\ell}/E_{n\ell}$, using (2.33) (Ericson 1970). The predicted ratios were compared to experimental values. For s- and p-waves, there was agreement, roughly within a factor of two. For d- and f-waves, taking experimental values for large nuclei (^{133}Cs and ^{238}U),

$$\left(\frac{\epsilon_{n\ell}}{E_{n\ell}}\right)_{\text{coherent}} \approx \left(\frac{\epsilon_{n\ell}}{E_{n\ell}}\right)_{\text{experiment}} \times 10^{-2} \quad (2.35)$$

so that the coherent sum of π^-N scattering in d- and f-states cannot account for the observed energy shifts. The interaction in these states is almost entirely due to the s- and p-wave interaction of the pion with the individual nucleons (Ericson 1970). Thus, in the

optical potential, d- and higher partial waves may safely be neglected.

This means that no matter what state the pion is in with respect to the nucleus, only s- and p-wave π -N interactions are considered to contribute to the total pion-nucleus interaction. The character of these interactions is strongly influenced by the granular structure of nuclear matter, which makes the s-wave interaction repulsive and leads to the Lorentz-Lorenz effect in the p-wave interaction (cf. Section 2.2.3).

To see how the s-wave interaction can be repulsive, consider an incident s-wave scattering off a single nucleon with scattering length $a_{\pi-n}$. In a first approximation, if the nucleus is homogeneous, s-wave scattering off the nucleus can be considered as the sum of scattering off the individual nucleons, with a potential (Backenstoss 1970)

$$V_N(\vec{r}) = \frac{-2\pi\hbar^2}{\mu_\pi} \left[\frac{Z}{A} a_{\pi-p} + \frac{A-Z}{A} a_{\pi-n} \right] \rho(\vec{r}) \quad (2.36)$$

As mentioned above, $a_{\pi-p} = b_0 - b_1$ is almost equal to $a_{\pi-n} = b_0 + b_1$, but with opposite sign, so that the two terms in $V_N(r)$ almost cancel. The remaining interaction is not nearly adequate to explain the observed 1s level shifts, so the assumption of a homogeneous nucleus must be replaced by including nucleon-nucleon correlations. The pion inside the nucleus sees the mass of a nearby nucleon as concentrated into a point, surrounded by a hole in the nuclear medium. The nuclear

pair correlation function gives the radius of the hole. The incident pion wave, $\phi_{n\ell}$, is replaced inside the hole by an effective field

$$\begin{aligned}\phi_{\text{eff}} &= \phi / (1 + a \langle \frac{1}{r} \rangle_{\text{corr}}) \\ &= \phi [1 - a \langle \frac{1}{r} \rangle_{\text{corr}} + \dots]\end{aligned}\quad (2.37)$$

where a is the π -N s-wave scattering length; a is then replaced by an effective s-wave scattering length

$$\begin{aligned}a_{\text{eff}} &= a [1 - a \langle \frac{1}{r} \rangle_{\text{corr}} + \dots] \\ &= a - a^2 \langle \frac{1}{r} \rangle_{\text{corr}} + \dots\end{aligned}\quad (2.38)$$

The linear term, as mentioned above, does not nearly account for the observed pion-nucleus s-wave interaction. The main contribution is from the a^2 term, which makes a_{eff} negative, giving the observed repulsive s-wave interaction. Pauli correlations, having the longest range, give the largest $\langle \frac{1}{r} \rangle$ and thus are the most important in this effect (Backenstoss 1970).

2.2.3 The Lorentz-Lorenz effect

The granularity of the nuclear medium also leads to an important modification of the p-wave term in the optical potential. Classically, dipole scattering of electromagnetic waves off the atoms in a gas produces a change in the refractive index when short-range atom-atom correlations are taken into account (the Lorentz-Lorenz effect). The dipole component in pion-nuclear scattering, which comes from the p-wave π -N scattering, produces a nuclear Lorentz-Lorenz effect when nucleon-nucleon correlations are taken into account.

In the derivation of this effect due to T. Ericson (Ericson 1970), the individual nucleons are taken to be point scatterers surrounded by holes cut out of the medium. The holes are considered to be small homogeneous spheres of radius R , with the pion p -wave field scattering off them. The wavefunction is required to be continuous at the surface of the spheres

$$\phi_-(R) = \phi_+(R) \quad (2.39)$$

The wavefunction is found by beginning with the wave equation

$$(\nabla^2 + k^2)\phi = 2m_\pi V\phi, \quad (2.40)$$

describing the propagation of the pion wave in a homogeneous medium under the influence of the potential V ; k is the pion momentum. Then, using the optical potential (2.24) for V , written in more compact form as

$$2m_\pi V(\vec{r}) = q(\vec{r}) + \vec{\nabla} \cdot \alpha(\vec{r}) \vec{\nabla} \quad (2.41)$$

where

$$\begin{aligned} q(\vec{r}) &= -4\pi a\rho(\vec{r}) \\ \alpha(\vec{r}) &= 4\pi c\rho(\vec{r}), \end{aligned}$$

the equation for $\phi(\vec{r})$ is obtained:

$$[\vec{\nabla} \cdot (1 - \alpha(\vec{r}) \vec{\nabla})]\phi + k^2\phi = q(\vec{r})\phi. \quad (2.42)$$

Integrating this equation along a line perpendicular to the surface of the sphere gives

$$(1 - \alpha) \left(\frac{d}{dr} \phi_- \right)_R = \left(\frac{d}{dr} \phi_+ \right)_R \quad (2.43)$$

where α is the dipole scattering strength; so far, $\alpha = 4\pi c\rho$ for completely uncorrelated scatterers. If R is small, the inside and

outside solutions are

$$\begin{aligned}\phi_- &= Ar^\ell Y_{\ell m} \\ \phi_+ &= B(r^\ell + br^{-\ell-1}) Y_{\ell m} .\end{aligned}\quad (2.44)$$

From (2.43),

$$\left[\frac{1}{r}(1-\alpha) \left(\frac{d}{dr} \phi_- \right) \right]_R = \left[\frac{1}{r} \left(\frac{d}{dr} \phi_+ \right) \right]_R \quad (2.45)$$

and using the solutions for ϕ_- and ϕ_+ , this gives

$$A(1-\alpha) \frac{\ell}{r} = B \frac{\ell - b(\ell+1)R^{-2\ell-1}}{R} . \quad (2.46)$$

From (2.39) and (2.44),

$$\begin{aligned}\frac{A}{B} &= 1 + bR^{-2\ell-1} \\ &= \frac{\ell - b(\ell-1)R^{-2\ell-1}}{\ell(1-\alpha)} \\ &= \frac{1}{\left(1 - \frac{\ell}{2\ell+1}\alpha\right)} .\end{aligned}\quad (2.47)$$

Therefore when an incoming wave scatters off the surface of the small sphere, the wave reaching the centre is a factor

$$\frac{1}{\left(1 - \frac{\alpha\ell}{2\ell+1}\right)}$$

smaller; in particular, this factor is

$$\frac{1}{1 - \frac{\alpha}{3}}$$

for p-waves.

In the derivation of the pion-nucleus optical potential (2.24), each nucleon is treated a fixed point scatterer, and then the scattering is summed over all nucleons in the nucleus using the

continuous nuclear densities $\rho_n(\vec{r})$ and $\rho_p(\vec{r})$. To take nucleon-nucleon correlations into account, each point scatterer can be considered to be surrounded by a hole in the medium, of radius equal to half the nucleon-nucleon correlation distance, filled with a plug of matter (the mass of the nucleon) at the centre. The field in the slot between the surface of the hole, and the plug, is just the pion field (2.40) propagating under the influence of the potential V produced by the scatterer at the centre. From (2.41) - (2.47), this field is stronger than the field inside the plug by a factor $(1 - \frac{\alpha}{3})$, for p-waves. In a homogeneous medium, such as the plug of matter at the centre of the hole, the p-wave field at any point is $\vec{\nabla}\phi$. Therefore, letting the size of the plug go to zero, i.e., in the limit of a point scatterer, the effective field inside the hole in the medium, at the point scatterer, is

$$\vec{E}_{\text{eff}} = (1 - \frac{\alpha}{3})\vec{\nabla}\phi . \quad (2.48)$$

The gradient or p-wave term in the optical potential, when no correlations were included, is just

$$\vec{\nabla} \cdot \alpha(\vec{r}) \vec{\nabla} \quad (2.49)$$

where

$$\alpha(\vec{r}) = 4\pi c \rho(\vec{r}) .$$

When nucleon-nucleon correlations are taken into account,

$$\alpha(\vec{r}) \rightarrow \alpha_{\text{eff}}(\vec{r})$$

the actual p-wave scattering strength. By replacing the p-wave field

in the homogeneous medium, $\vec{\nabla}\phi$, with the effective field, \vec{E}_{eff}

(2.50)

which gives

$$\begin{aligned}\alpha(\vec{r}) &= 4\pi c \rho(\vec{r}) \left(1 - \frac{\alpha(\vec{r})}{3}\right) \\ &= \frac{4\pi c \rho(\vec{r})}{1 + \frac{4\pi c \rho(\vec{r})}{3}}\end{aligned}\quad (2.51)$$

(Ericson 1970). The gradient term in the optical potential (2.24) then becomes

$$\vec{\nabla} \cdot \frac{\{c_0 \rho(\vec{r}) + c_1 [\rho_n(\vec{r}) - \rho_p(\vec{r})]\}}{1 + \xi \cdot \frac{4\pi}{3} \{c_0 \rho(\vec{r}) + c_1 [\rho_n(\vec{r}) - \rho_p(\vec{r})]\}} \vec{\nabla} \quad (2.52)$$

where ξ is the Lorentz-Lorenz parameter describing the strength of the effect; $\xi=0$ gives back the original gradient term, i.e., no correlations, and $\xi=1$ means very short range correlations are assumed.

In recent work by Powers et al. (Powers 1980), the parameter ξ was allowed to float freely in fits to pionic atom data. A preference for values of ξ greater than 1 was found, in conflict with earlier results. A possible theoretical justification was found in the inclusion of ρ -meson exchange effects (Brown 1976). However, the value of ξ obtained in the fits showed a strong sensitivity to the neutron radii used; the neutron radii were therefore kept fixed at Hartree-Fock values. Since neutron radii and ξ could not be determined simultaneously, further independent information about either one is

necessary before the question of the value of ξ can be resolved.

2.3 Pion absorption and nuclear medium effects

Pion absorption on one or more nucleons is an important feature of the pion-nucleus interaction that cannot be described in the general framework of multiple scattering theory. However, once the optical model potential has been obtained, absorption effects may be included by adding an imaginary part to the potential, in analogy with the partial wave scattering terms. Energy and momentum conservation require that pion absorption in a nucleus occur on at least two nucleons. Experimentally, it has been found that pion absorption in nuclei leads to the emission of two nucleons, anticorrelated in direction (Ericson 1970). This leads to the quasi-deuteron model, in which pion absorption is considered to occur only on np pairs in the nucleus with the same quantum numbers as the deuteron, and is considered to be the same process as pion absorption on free deuterons, except for scale factors. The absorption process is assumed to be short-ranged, so that the short-range part of the nuclear deuteron wavefunction is assumed to be the same as that of the free deuteron.

The threshold absorption rate for s-wave pions on free deuterons is $\beta_n |\phi_o(0)|^2$, where β_{11} is the absorption strength, and $|\phi_o(0)|^2$ is the probability of finding the neutron and proton simultaneously at the origin. The nuclear s-wave pion absorption rate is then proportional to $\frac{3}{4} \beta_{11} \rho_n \rho_p$, where the factor $\frac{3}{4}$ is the fraction of np pairs in the

nucleus with the same relative spin states as the deuteron. To this must be added pion absorption on pp pairs; this contributes less than 20%, scaled from the rates for π^- -production reactions such as $n+p \rightarrow p+p+\pi^-$. Also, p-wave pion absorption must be included.

Making the assumption that $\rho_n = \rho_p = \frac{\rho}{2}$, where ρ is the nucleon density, the absorptive terms added to the optical potential are (Ericson 1970)

$$-16\pi p_2 B_0 \rho_n \rho_p \cong -4\pi p_2 B_0 \rho^2$$

and

(2.53)

$$-16\pi p_2 C_0 \rho_n \rho_p \cong -4\pi p_2 C_0 \rho^2$$

where

$$p_2 = \left(1 + \frac{m_\pi}{2m_n}\right)^{-1}.$$

The factor p_2 transforms the coordinates to the π 2N centre of mass system. The imaginary parts of B_0 and C_0 are the s- and p-wave absorption strengths, and the real parts represent π 2N dispersion effects, i.e., the contribution to the potential from pion scattering off the nucleon pairs. The full pion-nucleus optical potential is then

$$V_N(\vec{r}) = \frac{-2\pi\hbar^2}{m_\pi} \{ p_1 b_0 \rho(\vec{r}) + p_1 b_1 [\rho_n(\vec{r}) - \rho_p(\vec{r})] + i p_2 B_0 \rho^2(\vec{r}) + \vec{\nabla} \frac{1}{f} (p_1 c_0 \rho(\vec{r}) + p_1 c_1 [\rho_n(\vec{r}) - \rho_p(\vec{r})] + i p_2 C_0 \rho^2(\vec{r})) \vec{\nabla} \}$$
(2.54)

where

$$f = 1 + \xi \cdot \frac{4\pi}{3} \{ p_1 c_0 \rho(\vec{r}) + p_1 c_1 [\rho_n(\vec{r}) - \rho_p(\vec{r})] + i p_2 C_0 \rho^2(\vec{r}) \}$$

Fits to pionic 1s states for elements from ${}^4\text{He}$ to ${}^{20}\text{Ne}$ by Tauscher and Schneider (1974) indicate that $\text{Re}B < 0$, i.e., that the $\pi 2N$ dispersion is repulsive, and also that $\text{Re}B_0/\text{Im}B_0 \cong -1$. Fits to pionic 2p states for elements from Al to Zn by Batty et al. (1979) indicate a positive $\text{Re}C_0$, and a ratio $\text{Re}C_0/\text{Im}C_0$ varying from 1.7 to 1.95, when the Lorentz-Lorenz effect is included. On the other hand, Powers et al. (1980) argue that increased precision in experimental results for pionic isotope shifts warrants including an isovector degree of freedom in the absorptive part of the potential. Thus, their absorptive terms are

$$\frac{-4\pi}{2\mu\pi} [B_0(\rho_n + \rho_p)\rho_p + B_1(\rho_n - \rho_p)\rho_p] \quad (2.55)$$

and

$$-4\pi [C_0(\rho_n + \rho_p)\rho_p + C_1(\rho_n - \rho_p)\rho_p] \quad (2.56)$$

where μ_π is the reduced mass of the pion. The real parts of B_0 , B_1 , C_0 , and C_1 are kept fixed at zero; the real contributions of these two-nucleon terms to the potential are considered to be included, to a first approximation, by redefining the single nucleon parameters so that, for example,

$$\text{Re}B_0 \langle \rho^2 \rangle + b_0 \langle \rho \rangle \approx b_0' \langle \rho \rangle . \quad (2.57)$$

The effect is to reduce the number of free parameters in the dispersive part of the potential by two, while increasing the number of free parameters in the absorptive part from two to four. Using this model, the fits to pionic atom level widths were indeed improved, and

gave non-zero values for the isovector absorptive parameters, $\text{Im}B_0$ and $\text{Im}C_0$.

In addition to pion absorption, further corrections to the optical model may be made to account for the effects of the nuclear medium. One important effect considered here is Pauli blocking. When a pion scatters off a nucleon in a nucleus, the Pauli principle requires that the nucleon scatter only into states not already occupied by the other nucleons, i.e., states having momenta greater than p_f , the Fermi momentum. For the s-wave isoscalar part of the optical potential, the correction has been estimated by Ericson and Ericson (1966) to be

$$\delta b_0 = \frac{3}{2\pi p_f} \left[\frac{\alpha_1^2 + 2\alpha_3^2}{3} \right] \quad (2.58)$$

where

$$b_0 = \frac{1}{3}(\alpha_1 + 2\alpha_3) - \delta b_0,$$

and δb_0 is large compared to b_0 . Tauscher and Schneider (1974) have included this correction in their optical model when fitting pionic atom data to obtain b_0 .

The influence of nucleon binding must also be taken into account, since the optical potential was developed assuming free nucleons. However, this correction is difficult to calculate, and it is not usually included explicitly. This effect and other unknown nuclear medium effects are taken into account by obtaining values of the optical potential parameters from fits to pionic atom data. The results may then be compared to the analogous parameters in free π^-N

scattering, to obtain an estimate of the magnitude of the nuclear medium effects, which include Pauli blocking and nucleon binding. Such global fits have been done by Tauscher and Schneider (1974), Batty et al. (1979), Powers et al. (1980), and Poffenberger et al. (1980).

2.4 The $^{16}, ^{18}\text{O}$ isotope pair

In the present experiment, the 1s level shifts and widths in pionic ^{16}O and ^{18}O were measured. The results are compared to another recent measurement made on the same isotope pair, and to a previous measurement made with a much lower energy resolution. The results are also included in a global fit to pionic atom 2p-1s data, to help determine optical model parameters more accurately. The ^{18}O results are particularly valuable in this respect because of their sensitivity to the isovector part of the optical potential; this sensitivity occurs in only two low-Z nuclei with observable 2p-1s transitions. This is especially important when testing for non-zero values of the isovector absorptive terms in the optical potential. Powers et al. (1980) introduced such terms into their potential, but included data on only two low-Z nuclei with appreciable isovector sensitivity, ^{18}O and ^{26}Mg , in their global fit.

In ^{16}O , charge symmetry implies that ρ_n is equal to ρ_p , neglecting Coulomb repulsion, so that the isovector terms in the optical potential are practically zero. Yet the many-body or nuclear medium effects are almost the same as in ^{18}O , so that the isotope shift

$$\epsilon_{1s}({}^{18}\text{O}) - \epsilon_{1s}({}^{16}\text{O})$$

and the difference in level widths

$$\Gamma_{1s}({}^{18}\text{O}) - \Gamma_{1s}({}^{16}\text{O})$$

reflect almost entirely the effects of adding two neutrons to a closed shell. While it should be possible to extract the neutron radius difference

$$\Delta r_n = r_n({}^{18}\text{O}) - r_n({}^{16}\text{O})$$

from this information, the interrelated dependence of the optical potential on the neutron radius and on the Lorentz-Lorenz parameter (Powers 1980) makes this unlikely at present, since the value of ξ is not well determined.

2.5 Pionic atom calculations: the program PIATOM

Theoretical predictions for the transition energies and level shifts and widths of pionic ${}^{16}\text{O}$ and ${}^{18}\text{O}$ were made using the computer code PIATOM (Krell 1977). This code is used to calculate numerically eigensolutions to the Klein-Gordon equation

$$\left\{ \nabla^2 + \frac{1}{\hbar^2 c^2} [(E - V_c)^2 - \mu_\pi^2 c^4] \right\} \psi = \frac{2\mu_\pi}{\hbar^2} V_N \psi \quad (2.59)$$

where

$$\mu_\pi = m_\pi \left(1 + \frac{m_\pi}{M} \right)^{-1}$$

$$M = A \left(\frac{m_n + m_p}{2} \right) .$$

The potential V_N contains the effects of finite nuclear size and optionally, of first order vacuum polarization. The pion-nucleus

optical potential V_N is given by (2.54).

An iterative procedure is used to find the complex energy eigenvalues $E_{n\ell}$ of (2.59), and an accuracy of one part in 10^6 in the eigenvalues is required for convergence. The real part of $E_{n\ell}$ is the level energy, and twice the imaginary part of $E_{n\ell}$ gives the level width

$$E_{n\ell} = \text{Re}E_{n\ell} + i\frac{\Gamma}{2} \quad (2.60)$$

Predictions of E_{2p-1s} , ξ_{1s} and Γ_{1s} were calculated for pionic ^{16}O and ^{18}O , with a set of optical potential parameters from the global fit to recent pionic X-ray data for light nuclei of Poffenberger (1980). The results are presented in Table XII together with the results of the present experiment. In Chapter V, the theoretical predictions and experimental results are compared and discussed.

CHAPTER 3

EXPERIMENTAL TECHNIQUE

3.1 Introduction

The experiment consisted of stopping pions in ^{16}O and ^{18}O targets and observing the resulting X-rays and gamma rays with a germanium solid state detector. The prompt energy spectra contained the pionic ^{16}O and ^{18}O 2p-1s X-ray lines, which were analyzed to obtain their energies, strong interaction shifts, and linewidths. The primary goal was a precise measurement of the differences between pionic ^{16}O and ^{18}O , with a view to drawing conclusions about differences in their nuclear structure. Therefore care was taken to keep experimental conditions as close to identical as possible when acquiring data with either target.

The measurement was performed at the TRIUMF stopped pion-muon channel M9, described below in Section 3.2 and shown in Figure 1. The arrangement of the experimental apparatus in the M9 area is shown in Figure 2. A telescope of plastic scintillators was used to detect the incoming pions and to define a pion stop in the target. Pions were stopped in one of two isotopically pure targets made of H_2O^{16} and H_2O^{18} . Three gamma ray sources were placed near the targets for an in-beam energy calibration. A hyperpure germanium solid state detector

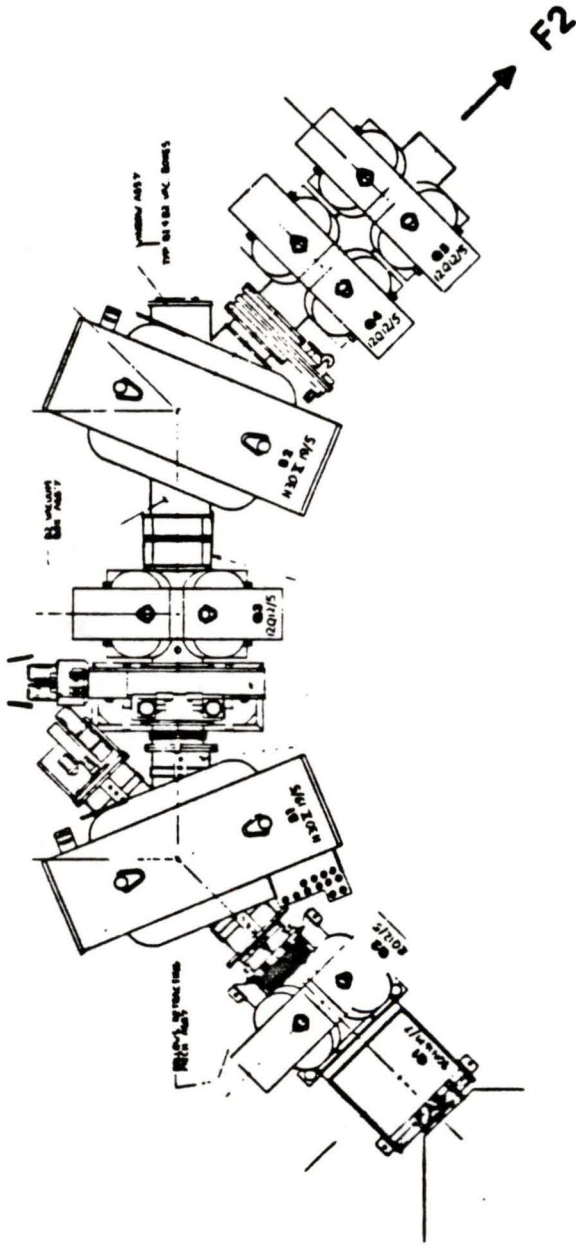
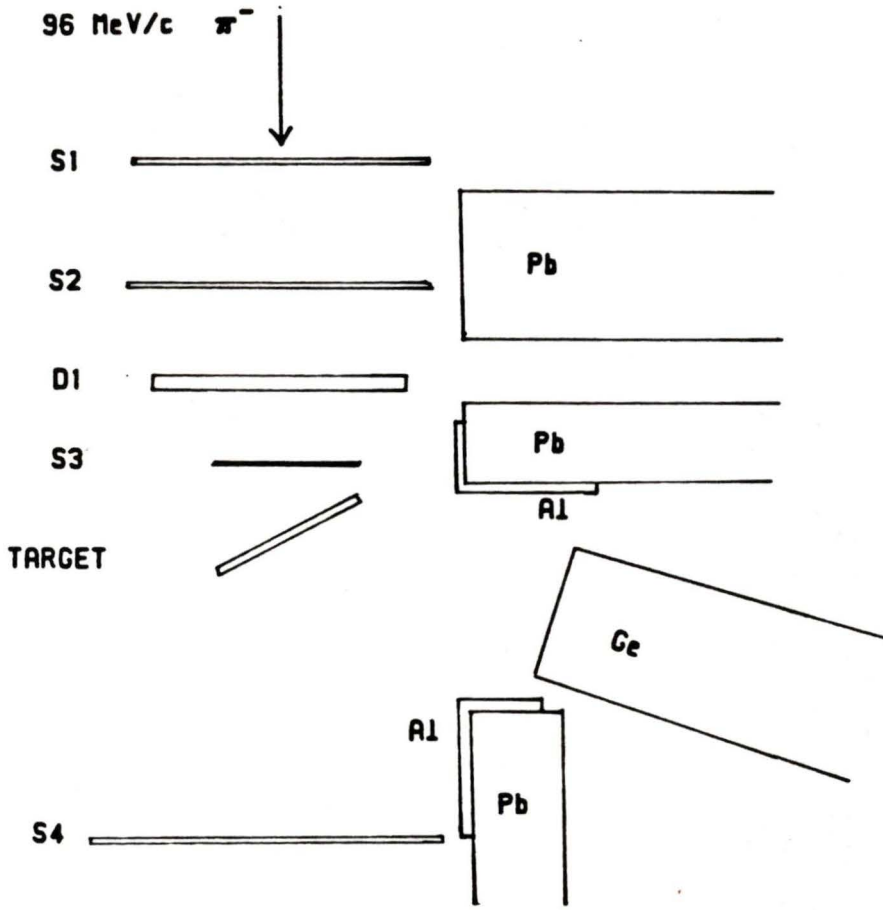


Figure 1. The M9 Channel.



Scintillator Dimensions

S1	10x10x.3 cm
S2	8x 8x.6 cm
S3	5x 5x.3 cm
S4	15x15x.3 cm

Figure 2. The Experimental Apparatus in the M9 Area.

was used to detect the X-rays and gamma rays coming from the target and calibration sources. The detector was shielded from the scintillators and other materials containing oxygen, in order to minimize the amount of ^{16}O seen by the detector while acquiring data with the ^{18}O target. The photon energies and times relative to pion stops were acquired and histogrammed on-line with a computer-based data acquisition system.

The measurement was performed April, 1979. It was repeated in October, 1979 in hopes of obtaining higher statistics, but severe lineshape distortion appeared in all the spectra. Because of this, only the data acquired in April, 1979 were used in the analysis.

3.2 The stopped pion channel

A brief description of the M9 channel is given here, following the description in the paper by Al-Qazzaz et al. (1980). A pulsed beam of up to 100 μA of 500 MeV protons extracted from the TRIUMF cyclotron strikes one of five pion production targets on the LAT2 ladder in beamline 1A, producing pions and electrons. Muons are produced near the target by pion decay. The targets available were 1 cm copper, which produces a smaller beam spot, and 10 cm beryllium, which gives greater pion flux. In this experiment the beryllium target was used throughout.

The 5 ns wide proton beam pulses strike T2 every 43 ns, producing pulses of secondary particles 43 ns apart. Focussing and bending magnets along the 8.2 m channel collect the secondary particles and deliver them as a beam with an achromatic focus at F2, where the

stopping target was located. The vertical plane phase space acceptance of the channel is set by vertical slits at F1. The momentum acceptance of the channel is controlled by a set of horizontal slits at F1, which give a momentum spread $\Delta p/p$ of about 1% per centimeter slit opening. The slit opening was set to 10 cm in the present experiment, so that the particles in the beam all had nearly the same momentum. Thus all the beam particles with the same mass travelled at approximately the same velocity and arrived at F2 at nearly the same time during every 43 ns beam pulse. The electrons, being the least massive, had the highest velocity and arrived first at F2. The muons arrived next, and the pions, being the most massive, arrived last. The flight time differences among the pions, muons and electrons were great enough that they arrived in distinct bunches in every beam pulse, producing the time-of-flight spectrum shown in Figure 3.

The muons in the beam, which come from pion decay anywhere in the channel, have a greater spread in momentum, for a given horizontal slit opening, than the pions or electrons arriving at F2. The momentum of muons coming from forward decays overlaps the momentum distribution of the pions, making it impossible to completely separate the pions from the muons by time-of-flight without losing a significant number of pion events. This is not always a disadvantage, since it allows observation of muonic X-ray lines, which may be used as energy calibration lines or as independent measurements of muonic X-ray transition energies. The intensity of muonic X-ray peaks in the prompt spectra may be controlled

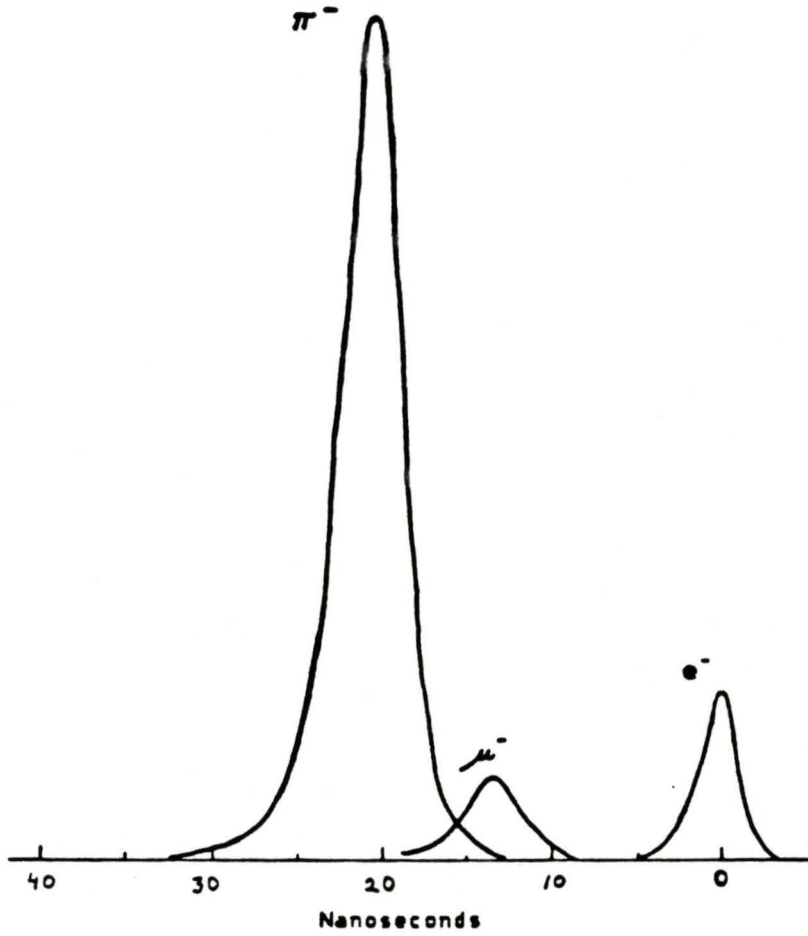


Figure 3. A Typical Time-of-Flight Spectrum for 100 Negative Particles in the M9 Stopped Pion-Muon Channel.

by varying the time-of-flight cutoff. In this experiment the cutoff was adjusted to give statistically significant muon peaks, whose centroids were fit to give muonic X-ray energies. Gamma ray sources were used for the energy calibration.

The momentum range of the M9 channel is 30 - 150 MeV/c. The channel was first tuned to 96 MeV/c, then fine-tuned during the course of the experiment to optimize the stopping rate of pions in the target. A typical range curve is shown in Figure 4. The master volts setting for the channel elements, which is linearly related to the channel momentum, was varied against the number of pion stops/primary proton beam intensity, until a maximum was obtained. This setting was kept until the target was changed, or until there was some change in the thickness of scintillators or degrader upstream of the stopping target.

The total negative particle flux at F2 was $5.5 \times 10^5 \text{ s}^{-1} \mu\text{A}^{-1}$ primary proton current. The channel momentum of 96 MeV/c gave a pion:muon:electron ratio of 65:5:30 (Al-Qazzaz 1980). The measured negative particle fluxes at F2 are shown in Table I.

The 10 cm beryllium pion production target would have produced a beam spot size at F2 about 2cm x 10cm if there had been no material between the end window and the stopping target. But scattering of the beam particles as they passed through two plastic scintillators, a 1.25 cm thick beryllium degrader, and finally the thin defining counter S3, produced a beam spot effectively the same size as the 5 cm x 5 cm

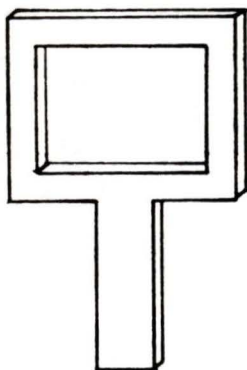


Figure 5. The Oxygen Target Holder.
 Dimensions: Outside 10cm x 8cm
 Inside 7cm x 5cm
 Thickness 3mm.

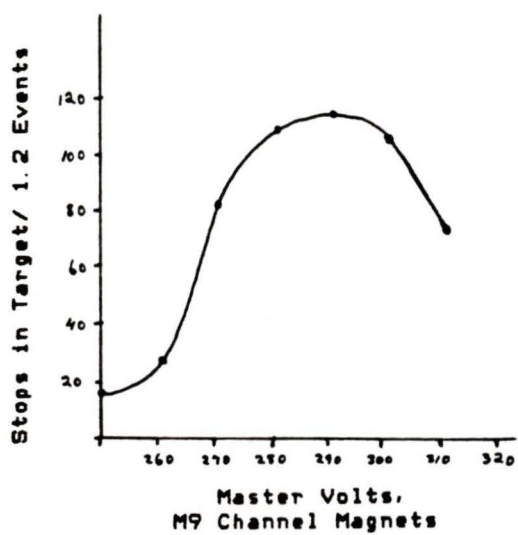


Figure 4. Range Curve in ^{18}O .

defining counter.

Table I			
Negative Beam Particle Fluxes at F2			
Primary Proton Beam Current	Total Particle Flux at F2 (1)	Pion Flux at F2 (2)	Muon Flux at F2 (3)
$10 \pm 3 \mu\text{A}$	$9 \times 10^5 - 1.6 \times 10^6$	$(5.0 - 8.7) \times 10^5$	$(0.3 \pm 0.1) \times 10^6$

(1) from the S1.S2 coincidence rate

(2) from the S1.S2. π coincidence rate

(3) estimated from the total particle flux using the ratio

$$\pi^- : \mu^- : e = 65 : 5 : 30$$

3.3 The scintillator telescope and event definitions

A standard four counter telescope was used to detect the incoming particles and to define a pion stop in the target. The counters were NE102 plastic scintillators coupled with light pipes to photomultiplier tubes. The scintillator dimensions and telescope geometry are shown in Figure 2.

A particle stop in the target was identified by a signal in counters 1, 2, and 3, but not in 4; i.e., $123\bar{4}$. To minimize the number of false stops caused by particles stopping in S3, the S3

scintillator was made very thin while still keeping good counting efficiency. Multiple scattering of beam particles in air between S3 and S4 resulted in a wide angular distribution, causing false stops by particles passing through S1, S2, and S3, but missing the target and then missing S4 as well. To minimize this kind of false stop, S3 was placed very close to the target, and its area was only slightly larger than that of the target. Also, the area of counter 4 was chosen to be large relative to the other counters.

Pions were distinguished from other particles stopping in the target by their flight time down the M9 channel. A time-of-flight spectrum such as the one shown in Figure 3 was produced by starting a time-to-amplitude converter with the 1.2 pulse, and stopping it with a pulse derived from either the cyclotron RF signal or a capacitive pick-up probe in beamline 1A. The time scale in Figure 3 runs from right to left, since the beam pulses originated in the cyclotron and ended up at S2. A logic pulse, called the π -gate, was set with sufficient delay and width to include most of the pion peak, and was "anded" with the $123\bar{4}$ pulse to produce the pion stop signal.

With the channel tuned to 96 MeV/c, the pions emerged from the end window with a kinetic energy of 30 MeV. This kinetic energy was reduced to nearly zero for the pions to stop in the target material. Since the three scintillators upstream of the target were not thick enough to do this, a 10 x 10 x 1.25 cm thick Be degrader (2.3 g/cm² thick) was placed between S2 and S3. Calculation of the degrader

thickness needed is shown in Appendix B. Since the pions travel through part of the target before stopping, the target thickness must be included in calculating the total amount of material needed to stop them. Since the two oxygen targets had different thicknesses, and the degrader thickness was fixed, it was necessary to retune slightly the channel each time the target was changed in order to maximize the pion stopping rate.

3.4 The oxygen targets Both targets were made of water: H_2^{16}O and H_2^{18}O . The H_2^{18}O target was made into a self supporting gel with agar. The H_2^{16}O target was liquid. The plastic target holders (Figure 5) were made of polythene frames with polystyrene windows and contained no more than 2% oxygen relative to the ^{18}O target mass. The H_2^{18}O was 0.52 g/cm^2 thick, with 1.5% agar. The H_2^{16}O was 2.0 g/cm^2 thick, with no agar. During the present experiment, the targets were interchanged approximately every ten hours.

Since the $\pi^{16,18}\text{O}$ 2p-1s X-rays were only about half their Lorentzian linewidths apart, any ^{16}O between S3 and S4 would produce a background peak under the $\pi^{18}\text{O}$ 2p-1s peak, whose intensity would be impossible to determine independently from a fit to the data. Therefore special care was taken to keep the amount of ^{16}O between S3 and S4 to a minimum. The ^{18}O target gel was put into the target holder in a nitrogen atmosphere. No paper was used in the S3 scintillator wrapping. The amount of oxygen in the 15 cm air path between S3 and S4 was estimated to be only about 1% of the mass of the target, so it was

decided not to place a bag of helium around the target. The lucite light pipe under S3 contained oxygen, but a pion would have to pass through S3 and then scatter into the light pipe before producing an X-ray which would appear in the prompt spectrum. The solid angle subtended by S3 to the light pipe was only about 20 msr, so the probability of such an event was negligible. There were also fixed percentages of ^{16}O and ^{17}O present in the ^{18}O . The manufacturer's specified isotopic purity was

^{18}O	97.47%
^{17}O	1.69
^{16}O	.84 .

The estimate of the total ^{16}O present during data acquisition with the ^{18}O target is detailed in Table II.

Table II
 Estimated Amount of ^{16}O Present during Data
 Acquisition with the ^{18}O Target

Source	Percent ^{18}O (of Total Oxygen Present)	Estimation Method
H_2O^{18}	0.84	specified isotopic purity
agar	$0.75 \pm .25$	chemical composition of the bacto-agar
air	$2.06 \pm .10$	comparison of the relative intensities of the πN 3-2 and πO 3-2 lines with the ratio of nitrogen to oxygen in air
target holder	$1.5 \pm .5$	chemical analysis of the plastics used; estimate of the ^{16}O content of the glue was nearly zero
Total	$5.15 \pm .85$	

The presence of ^{17}O and ^{18}O during data acquisition with the ^{16}O target was not a problem, since the relative amounts of these isotopes naturally present are small and fixed: for ^{17}O , 0.04%, and for ^{18}O , 0.2% of the total oxygen present.

3.5 Calibration sources

Gamma sources ^{75}Se , ^{182}Ta and ^{241}Am were placed near the target to provide an in-beam energy calibration. They were placed either just above or below the target, so that the gamma rays would not pass through the target before reaching the detector. The source event rate was related to the beam rate by requiring every source event to be in coincidence with a count from S5, a scintillation counter placed above the beam pipe, and in anti-coincidence with the π -stop pulse. The widths of the π -stop pulse and the gate from S5 were adjusted to make the prompt and source event acquisition rates approximately equal. This avoided the need for rate-dependent corrections to the detector resolution and efficiency functions, which were obtained from analysis of the source spectra, and then used in the analysis of prompt events.

3.6 The detector

The detector used in this experiment was an ORTEC planar hyperpure germanium detector. The bias voltage applied was -1000 V. The in-beam energy resolution was 712 ± 10 eV at 156 keV.

An excellent description of the workings of this type of detector is given in Goulding and Pehl, 1974. Photons passing through the germanium crystal deposit energy by creating electron-hole pairs, which

are collected at the electrodes when a bias voltage is applied across the crystal. The total charge of the output signal is proportional to the energy deposited, which will be the full energy of the incoming photon if it ejects a photoelectron, or some fraction of the energy if the photon Compton scatters and escapes without further interaction. At room temperature thermal excitation of electrons across the 0.7 eV band gap of Ge produces large numbers of electron-hole pairs, making the signals from incoming photons undetectable. Consequently, liquid nitrogen is used to cool the detector to 77⁰K, thus keeping the leakage current very low.

When germanium detectors are used as gamma ray spectrometers at energies greater than 30 keV, two major contributions to the energy resolution are the statistical nature of the electron-hole pair production and charge collection processes in the detector, and electronic noise in the external signal amplifying circuit. The two contributions may be combined in quadrature to give the FWHM (full width at half maximum) of the resulting spectral line

$$\Delta E = \sqrt{(\text{FWHM}_{\text{noise}})^2 + (2.35)^2(F\epsilon E)} \quad (3.1)$$

where ϵ is the average energy (eV) required to produce an electron-hole pair in the detector material (2.96 eV in germanium at 90⁰K), and F is the Fano factor, the fraction of energy deposited in the crystal which goes into non-ionizing processes (Goulding and Landis, 1974).

Charge trapping at impurities and defects in the crystal lattice

results in a loss of charge collected, producing an excess of events on the low energy side of the peak. Fluctuations in the amount of charge lost contribute further to broadening the peak. The amount of charge lost is almost proportional to the total charge produced, so the effect increases as the incoming photon energy increases.

To minimize damage to the detector crystal during the experiment from energetic particles - either scattered beam particles or fast neutrons produced by beam particles interacting with the surroundings - the detector was shielded from the beam path as shown in Figure 2. To shield the detector from lead X-rays produced in the shielding bricks by scattered beam particles, a 6 mm thick aluminum sheet was placed on the lead brick surfaces in sight of the detector.

3.7 The circuit logic and data acquisition system

A schematic drawing of the arrangement of the electronics, mostly NIM modules, used to define events and acquire data is shown in Figure 6. This arrangement, called the circuit logic, is divided into four sections: scintillator telescope; detector signal processing; event definition; and data acquisition.

3.7.1 Scintillator telescope

The scintillator telescope section of the circuit produces two gate pulses which are used to define events to be accepted by the data acquisition system. A "wide stop" pulse, 100 ns wide, results from a $1234\bar{4}$ coincidence, and defines a pion stopping in the target. A gate pulse from S5, the counter placed over the beam pipe, signals a

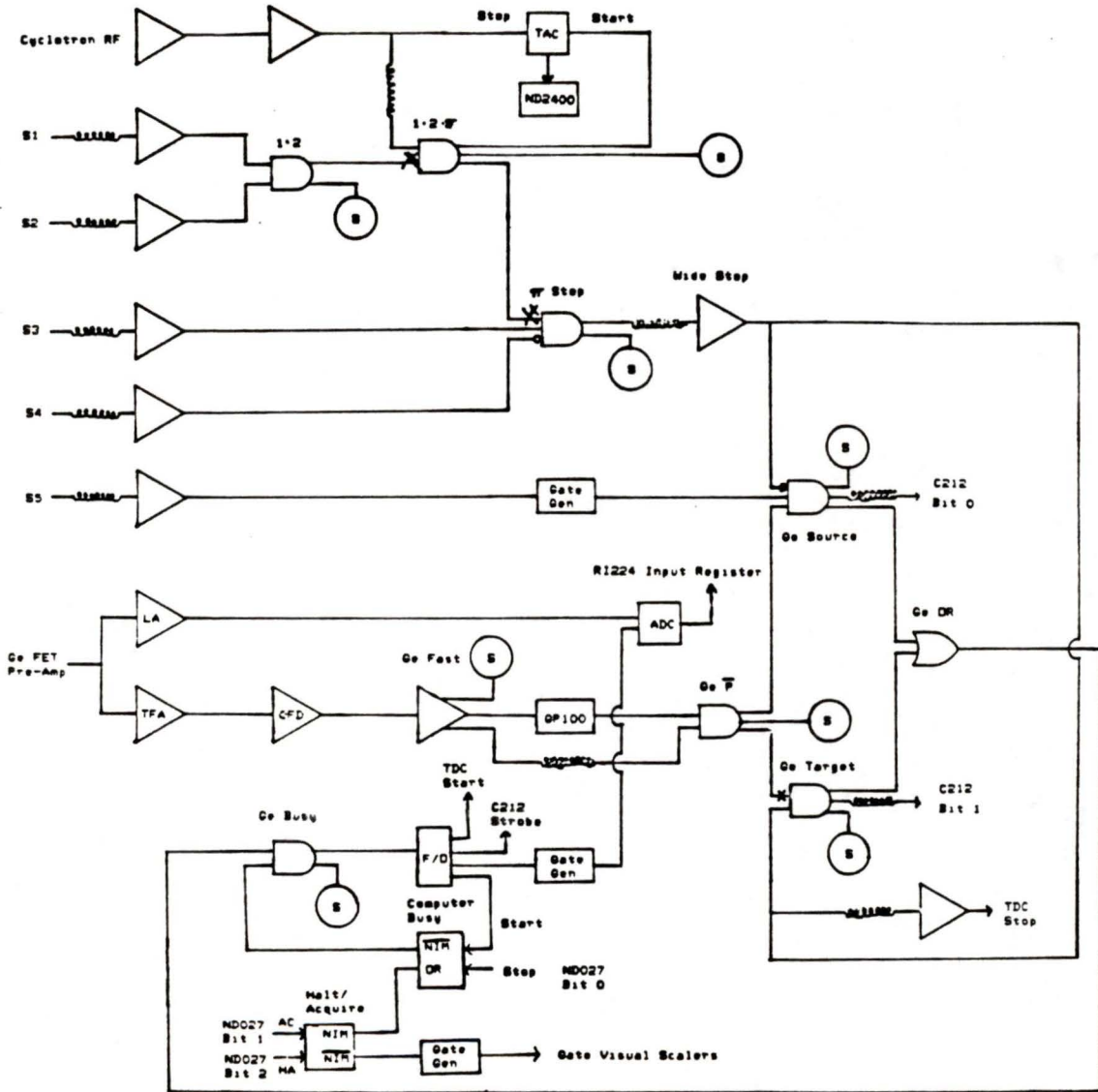


Figure 6. The Circuit Logic.

x : indicates that this input pulse carries the timing of target events in the detector.

beam-related event, and is used to gate the acceptance of source events by the data acquisition system. The width of the S5 gate pulse determines the number of source events accepted. It is adjusted to make the source and prompt pion stop event rates approximately equal, so that any rate-dependent effects on the lineshape will be the same for both prompt and source spectra.

3.7.2 Detector signal processing

The detector signal processing section of the circuit begins with a FET preamplifier which integrates and shapes the detector charge output that results from each incoming photon. The preamp output pulse has a long (about 50 microseconds) fall time, to achieve better linearity in the next stage of integration. This pulse is sent to two branches of the circuit: slow linear and fast timing. In the slow branch, a linear amplifier integrates and shapes the preamp output and produces a symmetrical Gaussian output pulse with voltage proportional to the original detector charge output. An ADC converts this pulse into an integer proportional to its voltage. The resulting pulse height distribution is linearly proportional to the incoming photon energy distribution seen by the detector.

The fast timing branch of the circuit eliminates pile-ups and produces a fast pulse which carries the timing of detector events. Pile-ups are detector events which occur so closely in time that they are processed as a single pulse by the linear branch of the circuit, so that their energy information is lost. The timing branch begins with a

timing filter amplifier which differentiates and amplifies the FET preamp pulse. Differentiation helps to eliminate timing walk caused by the variations in output risetime characteristic of Ge solid state detectors. The timing filter amplifier output goes to a constant fraction discriminator which almost completely eliminates the timing walk due to remaining variations in pulse height and shape. The constant fraction discriminator produces a fast timing output pulse, which is split - one pulse going to a pile-up gate, and the other delayed. The pile-up gate produces an output only if the timing pulse is not followed by another within the preset pile-up time. The delayed timing pulse and pile-up gate output are "anded" to produce a pile-up free signal which carries the timing of the original detector event.

3.7.3 Event definition

The event definition circuit sorts the detector events into two types, source and target, and signals the computer that an event has occurred. The source event gate "ands" the fast timing pulse with the complement of the wide stop, and with the beam-related S5 gate. Thus an output occurs only when a beam particle has passed through S5, a photon has deposited energy in the detector but no pion has stopped in the target. Most of these photons come from gamma ray sources placed close to the target for energy calibration. However, some source event photons come from pion and muon stops in materials surrounding the target: air, the target holder, the detector itself, and so on. Requiring accidental coincidence with the S5 gate ensures that the

source spectra are only acquired when there is beam on the target, so that any beam-related effects on the energy calibration will be the same for both source and prompt spectra.

The target event gate "ands" the fast timing pulse with the wide stop, producing an output only when a photon has been seen by the detector and a beam particle has stopped in the target. The ratio of pion to muon stops is controlled by the time-of-flight cutoff in the scintillator telescope section of the circuit. A target event gate output may be caused by a background event in accidental coincidence with a false wide stop, which is caused by a pion or muon passing through S1, S2 and S3, but missing the target and missing the veto counter S4 as well.

The two event gate outputs are "or-ed" to signal the computer that a valid detector event has occurred. Each event gate sets one of two bits in the CAMAC C212 unit which defines the type of spectrum in which the event will be stored.

3.7.4 Data acquisition

The data acquisition section of the circuit signals the computer to read the ADC, controls the acquisition of multiple timing spectra, provides a "computer busy" gate, and provides keyboard control of the ACQUIRE/HALT functions. The circuit begins with a gate which "ands" the detector event gate with the "computer busy" gate, thus producing an event trigger only when the computer is able to process an event.

The event trigger is fanned out four ways: to the C212 unit, which

sends a strobe to signal the computer to read the ADC; to a gate generator for the ADC, which ensures that the ADC only accepts pulses for conversion when the computer is able to read the ADC; to start the "computer busy" gate, which is stopped by the computer when an event has been processed.

Finally, the event trigger starts a TDC which is used to acquire multiple timing spectra. The TDC is stopped by the delayed wide stop, so that its output is proportional to the time difference between the particle stopping in the target and the resulting photon entering the detector. The computer reads and histograms the contents of the TDC, according to the energy of the incoming photon, as follows. The energy range of the detected incoming photons is divided into 16 equal intervals, and a separate histogram, or multiple timing spectrum, is produced for each energy interval. The multiple timing spectra are used to set the timing cuts which define the early, prompt and delayed energy spectra. The timing cuts are set separately for each energy interval to correct any energy-dependent timing walk. Since the time difference between target stop and detector event is different for pions and muons, the timing cuts must be set carefully to avoid differences in the ratio of pion to muon events in the prompt spectra from one energy interval to the next.

Keyboard control of the computer ACQUIRE DATA and HALT ACQUISITION functions is provided by a gate generator whose output is controlled by two bits in the ND027 unit, which are set when either AC or HA are

typed at the computer terminal. The AC/HA gate output goes to the "computer busy" gate, enabling or disabling data acquisition, depending on which command was typed in.

CHAPTER 4

ANALYSIS OF THE DATA

4.1 Introduction

The data acquired during the present experiment consisted of four types of spectra: prompt and delayed target event spectra, source event spectra, and multiple timing spectra. The multiple timing spectra were used on-line to separate target events into prompt and delayed spectra. The prompt spectra contained the lines of interest, the broadened pionic oxygen 2p-1s X-ray lines. The principal goal of the data analysis was to obtain the energies and linewidths of these X-rays.

The data were divided, according to target or to particular data acquisition conditions, into five different sets for separate analysis (Section 4.2). A least-squares peak-fitting program, JAGSPOT, was used to fit the X-ray lines (Section 4.3). The detector response function was unfolded from the spectral lines by the fitting program. The parameters of the response function - the energy resolution, detector efficiency, and low energy tailing - were obtained from fits to gamma ray lines in the source spectra (Section 4.4). The energy calibration was obtained by fitting gamma ray peak positions in the source spectra to a linear function, using precisely known values of the gamma ray energies (Section 4.5). The analysis of the principal lines of

interest in the prompt spectra, the broadened $\pi^{16}\text{O}$ and $\pi^{18}\text{O}$ 2p-1s X-rays, is discussed in Sections 4.6 - 4.7. The analysis of other lines of interest in the prompt spectra, the $\pi^{16,18}\text{O}$ 3d-2p and the $\mu^{16,18}\text{O}$ np-1s ($n \leq 5$) X-rays, is discussed in Sections 4.8 - 4.9.

4.2 Data acquisition

The measurement was first performed in April, 1979, then repeated in October, 1979. The October data were not analysed, due to severe lineshape distortion problems (cf. Section 3.1). The data acquired in April, 1979 were divided into five sets for separate analysis, according to the target used or to details of data acquisition. There were two sets of ^{16}O data. The first 60% was acquired without energy stabilization. The energy stabilizer, when used, compensated for gain drifts in the linear amplifier, thus preventing the shifting of spectral peak positions during data acquisition. Individual runs were saved and cleared every hour, but the gain drifted steadily, resulting in spectral peak shifts of about one channel (80 eV) per run, and worsening the resolution even within the runs. The gain had to be shifted and the dispersion changed for every run before it could be added to the others, contributing an additional uncertainty to the final results. The last 40% of the ^{16}O data was acquired using a stabilizer. There were no significant gain drifts (less than ± 0.4 spectrum channels, or 30 eV, over all runs) and these data were used in the final analysis.

There were three sets of ^{18}O data. The first 17% was acquired

before the cyclotron shutdown. When data acquisition was restarted eight days later, the gain and dispersion of the new spectra were so different from the previous data (spectrum peak positions had changed by up to 70 channels) that the early set of data had to be analyzed separately. The next 40% of the ^{18}O data were acquired while the ADC was setting the contents of every other channel to zero, at first intermittently, then steadily. Adding every two neighboring channels produced smoothed spectra with resulting loss of lineshape information (the peak FWHM at 150 keV was only four channels), contributing additional uncertainty to the final results. When the final 43% of the ^{18}O data was taken, the ADC was functioning properly and the spectra showed no apparent problems. This set of data was used in the final analysis.

4.3 The peak fitting program

The peak fitting program used was JAGSPOT, originally a gamma ray fitting program developed at Chalk River (Olin 1978). It was modified specifically to make it suitable for the analysis of pionic X-ray spectra, and to run on the IBM 370 Conversational Monitor System (CMS) at the University of Victoria. The modifications included the addition of a Gauss-Lorentz convolution to fit broadened pionic X-rays, the optional fitting of low energy exponential tails, and the optional folding of the detector efficiency function with the lineshape fitting function.

The general form of the lineshape fitting function is

$$\phi(x_i, \bar{a}) = a_1 + a_2 x_i + b(x_i) + \sum_{j=1}^N a_{2j+3} f_{\alpha_j}(x_i - a_{2j+4}) \varepsilon(x_i) \quad (4.1)$$

where x_i is the channel number, \bar{a} is the set of fitting parameters a_k , $b(x_i)$ the tailing function, N the number of peaks in the window, f_{α_j} the lineshape function, and $\varepsilon(x_i)$ the detector efficiency function. The best values of the parameters a_k are obtained by using a least-squares fitting method to minimize χ^2 ; the Marquardt-Levinson algorithm is used for its robust convergence properties (Olin 1978).

The first three terms in (4.1) represent the spectrum background. The terms in a_1 and a_2 represent a linear background. A quadratic term is not used because the major non-linear contribution to the background, the detector tailing, is included in $b(x_i)$, given by

$$b(x_i) = a_{25} \sum_{j=1}^M (y_j - d_j) e^{-a_{26}(x_j - x_i)} \quad (4.2)$$

$$d_j = a_1 + a_2 x_j + b(x_j)$$

where y_j is the number of counts in channel x_j , and M , the number of channels in the fitting window.

The functions f_{α_j} are the individual peak shapes. Two types of peak shape were used in the present analysis. The first, a Gaussian,

$$f_1(x) = e^{-a_3 x^2} \quad (4.3)$$

represents the response of the detector to a strictly monoenergetic photon. The finite width is due to the statistics of ionization and charge collection in the detector, and to electronic noise. The second

function is a convolution of the Gaussian detector response with a Lorentzian lineshape

$$f_2(x) = \int_{-\infty}^{\infty} \frac{\exp[-a_3(x-x')^2]}{a_{29}^2 + x'^2} dx' \quad (4.4)$$

where the Lorentzian

$$\frac{1}{a_{29}^2 + x'^2}$$

represents a transition with finite natural linewidth a_{29} - for example, a broadened pionic X ray.

The detector efficiency is not a constant characteristic of the detector, but must be measured separately for each experiment. It varies according to experimental conditions, and according to the immediate past history of the detector, e.g., how much neutron damage has been sustained. The measured efficiency is fit to an appropriate function $\epsilon(x_i)$, which is written into the fitting program as a separate section of code. In the general form of the lineshape (4.1), the term $\epsilon(x_i)$ is optional, and is only used with a Lorentzian lineshape, since it represents the peak shape resulting from a single transition with a finite spread in energy. The detector efficiency variation over the incoming photon energy range affects the peak shape, and significantly so if the variation is more than a few percent over the peak width. In the present experiment the effect is significant: the broad pionic ^{16}O and ^{18}O X-ray peaks are about 5 - 8 keV wide, the detector efficiency varies by about 7% over their widths, and the

fitted peak energies change by about 100 eV when the efficiency function is included in the lineshape.

4.4 The detector response function

The detector response function had three components: the energy resolution, the detector efficiency as a function of energy, and the low energy tailing function. The energy resolution and tailing functions were determined from fits to gamma ray lines in the source spectra, because these lines have well-known energies and nearly zero natural linewidths. The detector efficiency function was determined from fits to a series of gamma rays in the source spectra whose relative intensities are well known.

The energy resolution was obtained by fitting the FWHM of six peaks in the source spectra to the expression (cf. Section 3.6)

$$[\text{FWHM (keV)}]^2 = a_1 + a_2 E(\text{keV}) \quad (4.5)$$

where a_1 and a_2 are, respectively, the contributions of electronic noise in the external circuit, and of statistical processes in the detector. The peaks used in the fit are shown in Table III; the gamma ray energies are from Helmer et al., (1978). The detector energy resolution as a function of energy is shown in Figure 9. The best fit gave $a_1 = 0.147 \pm 0.010$ keV, $a_2 = 0.00231 \pm 0.00005$ keV. From this fit the resolution at 155 keV was 711 ± 8 eV.

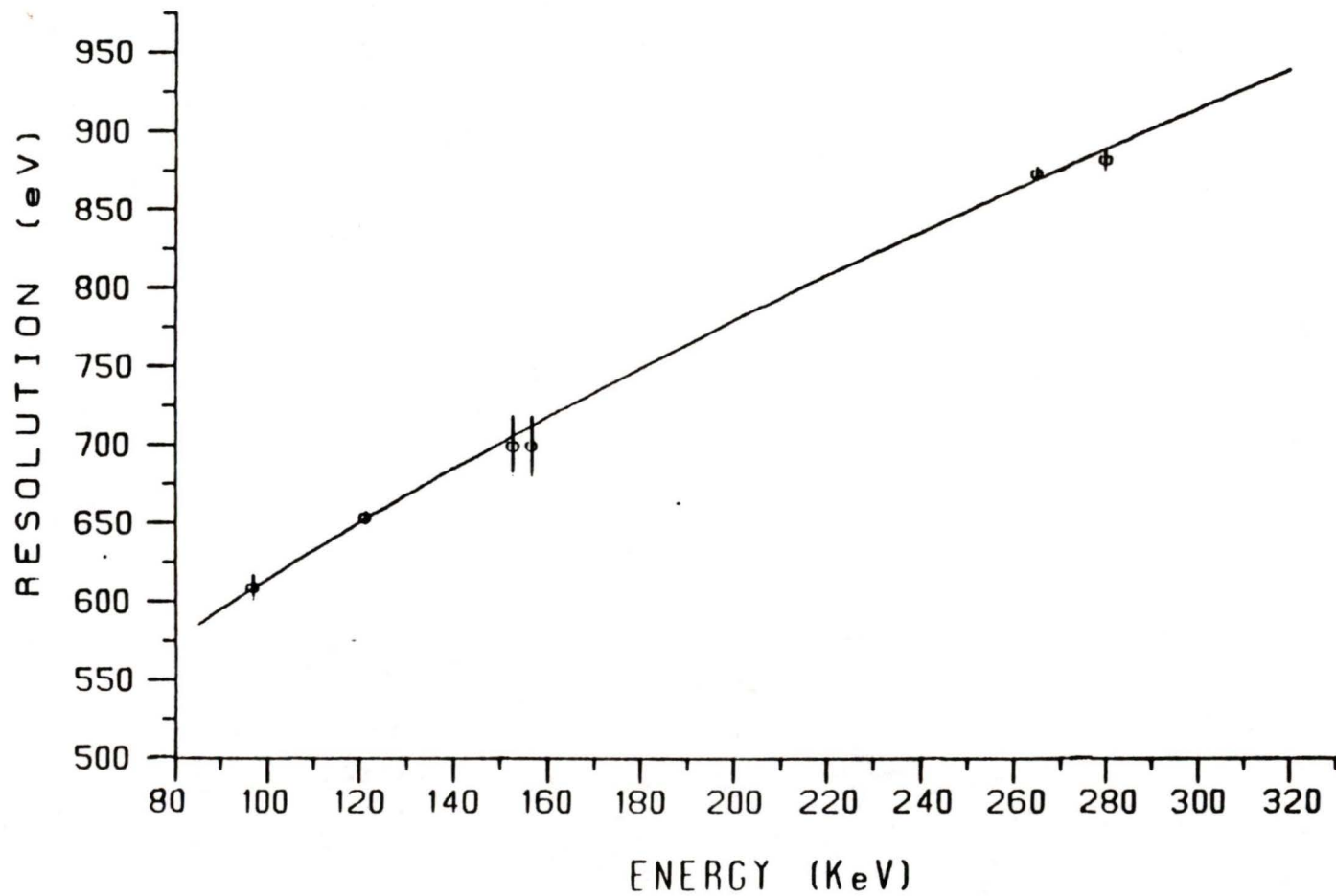


Figure 7. Detector Energy Resolution vs X ray Energy.

Table III
Peaks Used to Determine the Detector Energy Resolution

	Energy (keV)	FWHM (eV)
γ ^{75}Se	96.734 (.002)	608.7 (7.8)
γ ^{75}Se	121.119 (.003)	653.0 (3.7)
γ ^{182}Ta	152.4308 (.0002)	699.3 (18.8)
γ ^{182}Ta	156.3874 (.0003)	699.3 (18.8)
γ ^{75}Se	264.656 (.004)	873.5 (3.9)
γ ^{75}Se	279.538 (.003)	882.5 (6.6)

The detector efficiency function was obtained by fitting the measured intensities of six of the ^{75}Se gamma ray peaks in the source spectrum to an appropriate analytical function. The relative intensities of ^{75}Se gamma rays have been precisely measured (Gehrke 1977). The measured intensities, $I(E)$, of the peaks in the source spectrum were combined with the relative intensities, $I_R(E)$, of Gehrke et al. (1977), to define the relative efficiency of the detector at the energy E

$$\epsilon(E) = \frac{I(E)}{I(E_{\text{std}})} \frac{I_R(E_{\text{std}})}{I_R(E)} \quad (4.6)$$

The relative intensities of Gehrke (1977) are normalized to the 264 keV line. In the present analysis, the 121 keV line was chosen as the efficiency standard ($E_{\text{std}} = 121.119$ keV), because its fitted intensity had a small error and it was close to the energy region of interest, 150-160 keV.

The values obtained for $\epsilon(E)$ were fit to several functional forms. The function which gave the best fit was

$$\epsilon(E) = a_1 e^{a_2 E} \quad (4.7)$$

with $a_1 = 3.21$ and $a_2 = -0.00961$ keV⁻¹. The peaks used, and their intensities, are shown in Table IV. The relative efficiency of the detector as a function of energy is shown in Figure 8.

The energy dependence of self-absorption of X-rays in the target material was calculated as a possible correction to the detector efficiency function, but the differences in self-absorption across the full width of both broadened pion peaks were found to be less than 0.2%, and were therefore neglected.

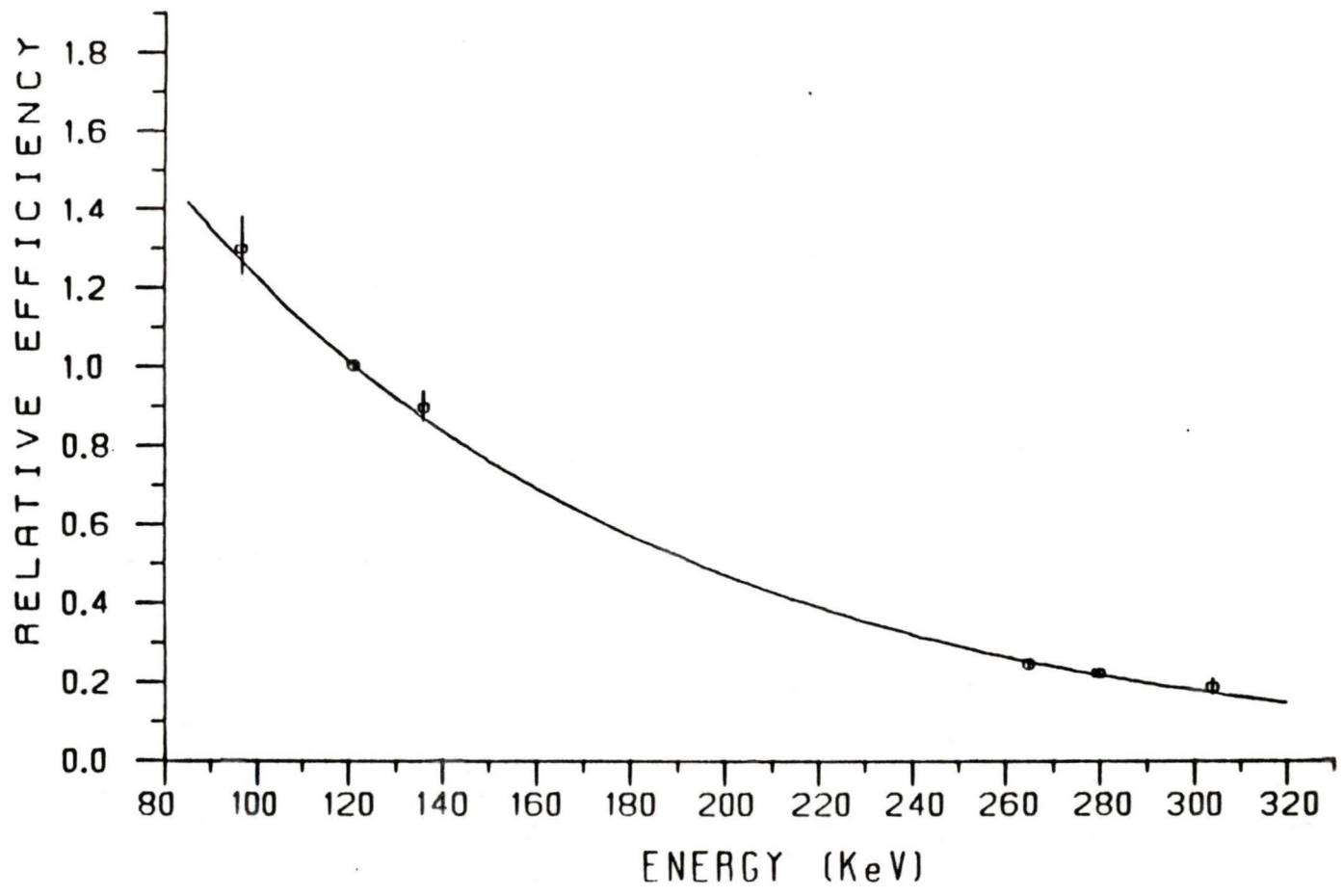


Figure 8. Detector Efficiency vs X ray Energy.

Table IV
⁷⁵Se Gamma Ray Peaks Used to Determine the Detector
 Efficiency Function

Energy (keV)	Measured Intensity (Peak Area)	Relative Intensity (1)
96.734 (.002)	14119 (180)	5.9 (0.3)
121.119 (.003)	54718 (396)	29.8 (0.9)
136.002 (.003)	167690 (547)	102. (0.3)
264.656 (.004)	44966 (240)	100. (0.3)
279.538 (.003)	17324 (145)	42.4 (1.3)
303.924 (.003)	757 (45)	2.21(0.03)

(1) from Gehrke et al. (1977); normalized to the 264 keV peak.

The parameters of the low energy tailing function (4.2) were obtained by fitting gamma ray peaks in the source spectra. The peak statistics were not high enough to allow the simultaneous determination of both tailing parameters, so a series of fits was made, in which the two parameters were alternately floated and fixed. Making the tail areas very low always worsened χ^2 , but in general the χ^2 minima with respect to variations in tail area or shape were very flat. Some

typical values of best fit tailing parameters are shown in Table V.

	Energy (keV)	Tail Area (% of Total Peak Area)	Tailing Amplitude (a_{25})	Exponential Decay Constant (a_{26})
$\gamma^{75}\text{Se}$	96	7.0	0.0127	0.1823
$\gamma^{75}\text{Se}$	121	13.3	0.0400	0.3013
$\gamma^{75}\text{Se}$	136	7.0	0.0127	0.1823
$\gamma^{182}\text{Ta}$	152	15.9	0.0313	0.1965
$\gamma^{182}\text{Ta}$	156	15.9	0.0313	0.1965
$\gamma^{75}\text{Se}$	264	15.9	0.0313	0.1965
$\gamma^{75}\text{Se}$	279	15.9	0.0313	0.1965

When fitting the broadened pion peaks at 155-160 keV, $a_{25} = 0.0313$ and $a_{26} = 0.1965$ were used. These parameters gave a good representation of the lineshape over the entire energy range.

4.5 The energy calibration

The energy calibration was obtained by fitting the peak positions of the best-determined lines in the source spectra both to a linear

and a quadratic function, using the least-squares method. The quadratic term was very small, of the order of 10^{-8} , in all the fits, thus the linear calibration was used.

The calibration function was

$$E(\text{keV}) = a_1 + a_2 \times \text{Channel} \quad (4.8)$$

with the best fit values $a_1 = 7.2747 \pm 0.0068$ keV, and $a_2 = 0.081827 \pm 0.000002$ keV/Channel. The peaks used in the calibration are listed in Table VI. The gamma ray energies are from Helmer et al. (1978). The calibration curve is shown in Figure 9.

4.6 Analysis of the pionic ^{18}O 2p-1s X-ray line

The first step in the analysis of the $\pi^{18}\text{O}$ 2p-1s X-ray line was a preliminary fit to obtain the energy of the line to within approximately 1%. The fitted energy was 156 ± 1 keV. The energy resolution and the tailing function parameters were fixed to their values at this energy, in all subsequent fits. The resolution was fixed at 712 eV, the parameters of the tailing function (4.2), at $a_{25} = 0.03134$ and $a_{26} = 0.1965$.

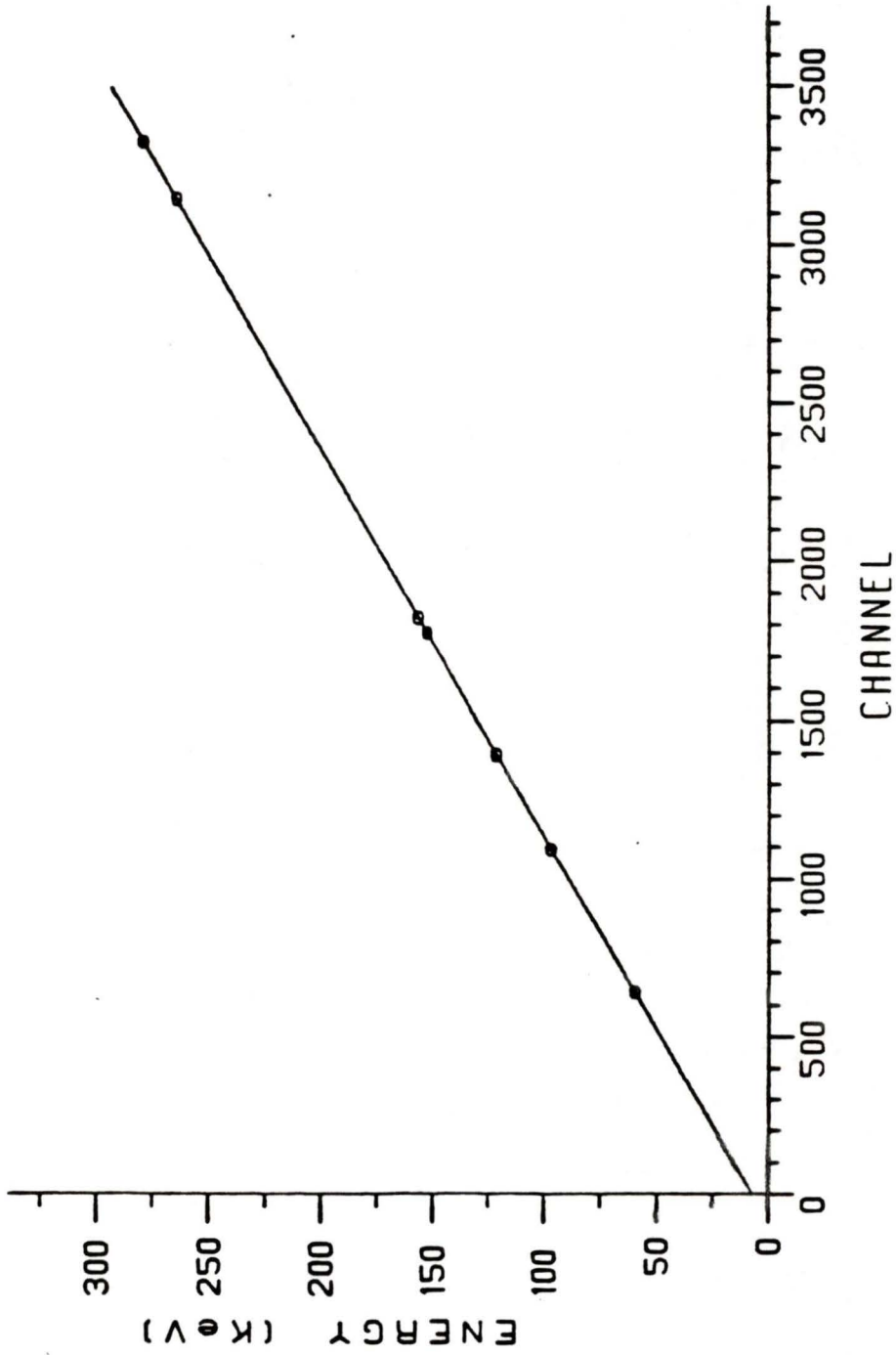


Figure 9. The Energy Calibration Curve.

Table VI
Peaks Used to Determine the Energy Calibration

	Energy (KeV)	Channel	Fitted Energy (keV)
$\gamma^{241}\text{Am}$	59.537 (.001)	638.90 (.30)	59.554 (.025)
$\gamma^{75}\text{Se}$	96.734 (.002)	1093.29 (.06)	96.735 (.006)
$\gamma^{75}\text{Se}$	121.119 (.003)	1391.20 (.08)	121.112 (.007)
$\gamma^{182}\text{Ta}$	152.4308 (.0002)	1773.96 (.18)	152.433 (.015)
$\gamma^{182}\text{Ta}$	156.3874 (.0003)	1822.46 (.26)	156.401 (.021)
$\gamma^{75}\text{Se}$	264.656 (.004)	3145.45 (.04)	264.658 (.003)
$\gamma^{75}\text{Se}$	279.538 (.003)	3327.29 (.06)	279.536 (.005)

The lineshape function used in fitting the $\pi^{18}\text{O}$ 2p-1s X-ray was the Gauss-Lorentz convolution (4.4). The detector efficiency $\epsilon(E)$ was included in the lineshape, as in (4.1). The effect of including the detector efficiency in the fits was to increase the fitted peak energy by 121 eV, and the fitted Lorentzian width by 87 eV.

The background was fitted as a linear function, since in fitting the source spectra it was found that adequate fits to the tailing function left the remaining background very linear. Both slope and intercept were always floated. A test was made for a possible

additional contribution to the background, a Compton edge from a higher energy peak. A search was made of the prompt spectra for peaks in the 273-314 keV range, which produce Compton edges in the 141-173 keV fitting window for the $\pi^{18}\text{O}$ 2p-1s line. However, no such peaks were found.

The peaks in the fitting window are listed in Table VII. The prompt spectrum in the region of the fitting window is shown in Figure 10. The gamma ray line at 169 keV was due to inelastic neutron scattering in ^{12}C , in scintillator S3 and in the target holder plastic. The πCl 3d-2p line came from pion stops in the polyvinylchloride in the tape used in scintillator wrapping. This line was fitted with its position and Lorentz width fixed at the measured values $E = 150.55 \pm 0.15$ keV, $\Gamma = 0.89 \pm 0.25$ keV (Poth 1979); its intensity was allowed to float.

The positions of the $\pi^{16}\text{O}$ 2p-1s and $\pi^{17}\text{O}$ 2p-1s peaks were fixed. The intensity of the $\pi^{17}\text{O}$ 2p-1s peak was fixed at about 1.7% of the total oxygen present, to allow for the 1.69% from the H_2O impurity and the .04% naturally present in oxygen. The intensity of the $\pi^{16}\text{O}$ 2p-1s line was first fixed at 5.15% of the total oxygen present,

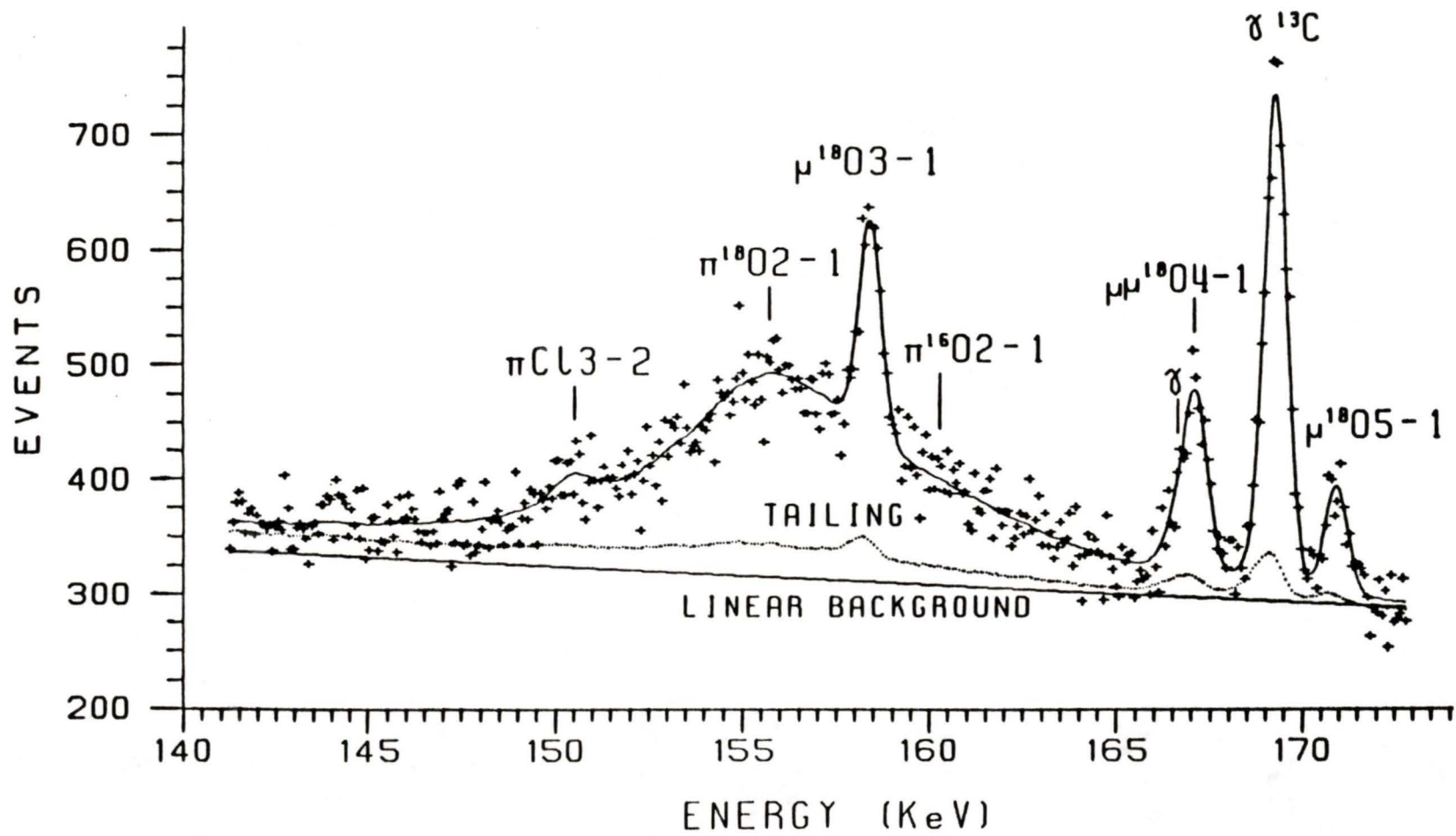


Figure 10. The $\pi^{18}O$ 2p-1s Fitting Window.

Table VII
Peaks in the Fitting Window of the $\pi^{18}\text{O}$ 2p-1s X-ray

Peak	Energy (keV) (1)	Intensity (events)
πCl 3d-2p	150.489 (.006)	487 (139)
$\pi^{18}\text{O}$ 2p-1s	155.792 (.105)	14962 (965)
$\pi^{17}\text{O}$ 2p-1s	158.184 (.006)	388 fixed
μO 3p-1s	158.422 (.023)	1624 (100)
$\pi^{16}\text{O}$ 2p-1s	160.286 fixed	5163 fixed (2)
	166.604 (.006)	311 (160)
μO 4p-1s	167.148 (.046)	1316 (164)
$\gamma^{13}\text{C}$	169.292 (.011)	3675 (97)
μO 5p-1s	170.933 (.035)	820 (77)

(1) Errors listed are statistical.

(2) The $\pi^{16}\text{O}$ 2p-1s intensity was varied (cf. Section 4.6) while testing for the amount of ^{16}O present; in the fit used to obtain the present results, it was fixed at the value listed here.

according to the estimate detailed in Table II. The intensity was then allowed to float. The resulting fit converged in about the same number of iterations as the previous fit, the χ^2 per degree of freedom

decreased from 1.02 (with 5.15% ^{16}O) to 0.97, and the fitted intensity of the $\pi^{16}\text{O}$ 2p-1s line was 33.1% of the total number of πO 2p-1s events. The energy of the $\pi^{18}\text{O}$ line was 680 eV less than in the previous fit (with 5.15% ^{16}O), and the Lorentz width had decreased by 2.42 keV. Apparently the percentage of ^{16}O assumed to be present had significant effects on the fit, so it was investigated further.

Various possible contributions to the ^{16}O present while taking data with the ^{18}O target were considered and tested for; the results of all except the contribution of the H_2^{18}O impurities are summarized in Table II. A mass spectrometer test of the ^{18}O target gel could not be done because the original target was no longer available. A mass spectrometer test on a target gel similarly prepared with H_2^{18}O from the same source (the Los Alamos Meson Production Facility, LAMPF), was done by the University of British Columbia Department of Chemistry. The result was a ^{16}O content of 21+5% of the total oxygen in the gel. On the other hand, the LAMPF Chemistry Department's test results gave about 0.5% ^{16}O content of the water used in preparing the gel (the "manufacturer's specified isotopic purity"). This serious inconsistency in the two results points to the possibility that the H_2^{18}O was contaminated with ^{16}O while it was being made into a gel, either through contact with water vapor or through air dissolving in the H_2^{18}O . It is also possible that contamination of the gel may have occurred, through contact with water vapour in the air, during long storage periods; however, this is not very likely, since exchange

of water molecules takes place very slowly between solid materials and air.

Since there is no conclusive evidence to support either hypothesis, an attempt was made to obtain independent evidence, from peaks in the prompt spectra, of the amount of ^{16}O present. Three possibilities were tried. The ratio of the areas of the πN 3d-2p and the πO 3d-2p lines was multiplied by the relative abundance of oxygen in air to give the percent of ^{16}O events from pion stops in the air path between S3 and S4; this gave a lower limit on the total ^{16}O present of $^{16}\text{O}_{\text{air}} = 0.021$ of the total $^{16},^{18}\text{O}$. The second possibility was analysis of the $\mu^{18}\text{O}$ 2p-1s X-ray line as a hyperfine complex, with components from $\mu^{18}\text{O}$ and $\mu^{16}\text{O}$, to obtain the relative intensity of the $\mu^{16}\text{O}$ events. However, the spacing between the components was less than half a channel (40eV), and this proved to be too small a separation for resolution by the peak fitting program. Also, the peak was on a boundary between two timing cut regions. The slightly different pion to muon intensity ratios on either side of the boundary created a small step in the background directly under the peak, which contributed an additional uncertainty to the fit. The third possible test was analysis of the $\pi^{18}\text{O}$ 3d-2p X-ray line for the intensity of the ^{16}O component. The two isotopic components were, however, too closely spaced for resolution by the fitting program, although there was possible evidence for a significant ^{16}O component in the fitted width, which was larger than the theoretical prediction by

nearly a factor of ten. Details are discussed in Section 4.8.

In summary then, the evidence on the percentage ^{16}O contamination of the ^{18}O target is not conclusive. The final estimate of the amount of ^{16}O present, as a percent of the total oxygen present during data acquisition with the ^{18}O target, was

$$\begin{aligned} \text{H}_2^{18}\text{O} \text{ isotopic impurity} &: 21.0 \pm 5.0 \% \\ \text{all other} &: 4.3 \pm .8 \% \end{aligned}$$

(air, target holder and agar)

$$\text{Total} : 25.3 \pm 5.1 \% .$$

The relative intensity of the $\pi^{16}\text{O}$ 2p-1s line in the $\pi^{18}\text{O}$ 2p-1s fitting window was fixed at this value in the final analysis. Results are shown in Table VII. The various contributions to the uncertainty of the final results are shown in Table X.

4.7 Analysis of the pionic ^{16}O 2p-1s X-ray line

The analysis of the $\pi^{16}\text{O}$ 2p-1s line was very similar to that of the $\pi^{18}\text{O}$ 2p-1s line. The lineshape parameters at the preliminary peak energy of about 160 keV were determined and then fixed. The resolution at 160 keV was 719 ± 8 eV; the tailing parameters were fixed at the same values as for the $\pi^{18}\text{O}$ fit. The detector efficiency function was included in the lineshape. The background was fitted to a linear function; no high energy lines were found in the prompt spectrum which could produce a Compton edge in the fitting window.

The peaks in the fitting window are listed in Table VIII. The prompt spectrum in the fitting window is shown in Figure 11. The

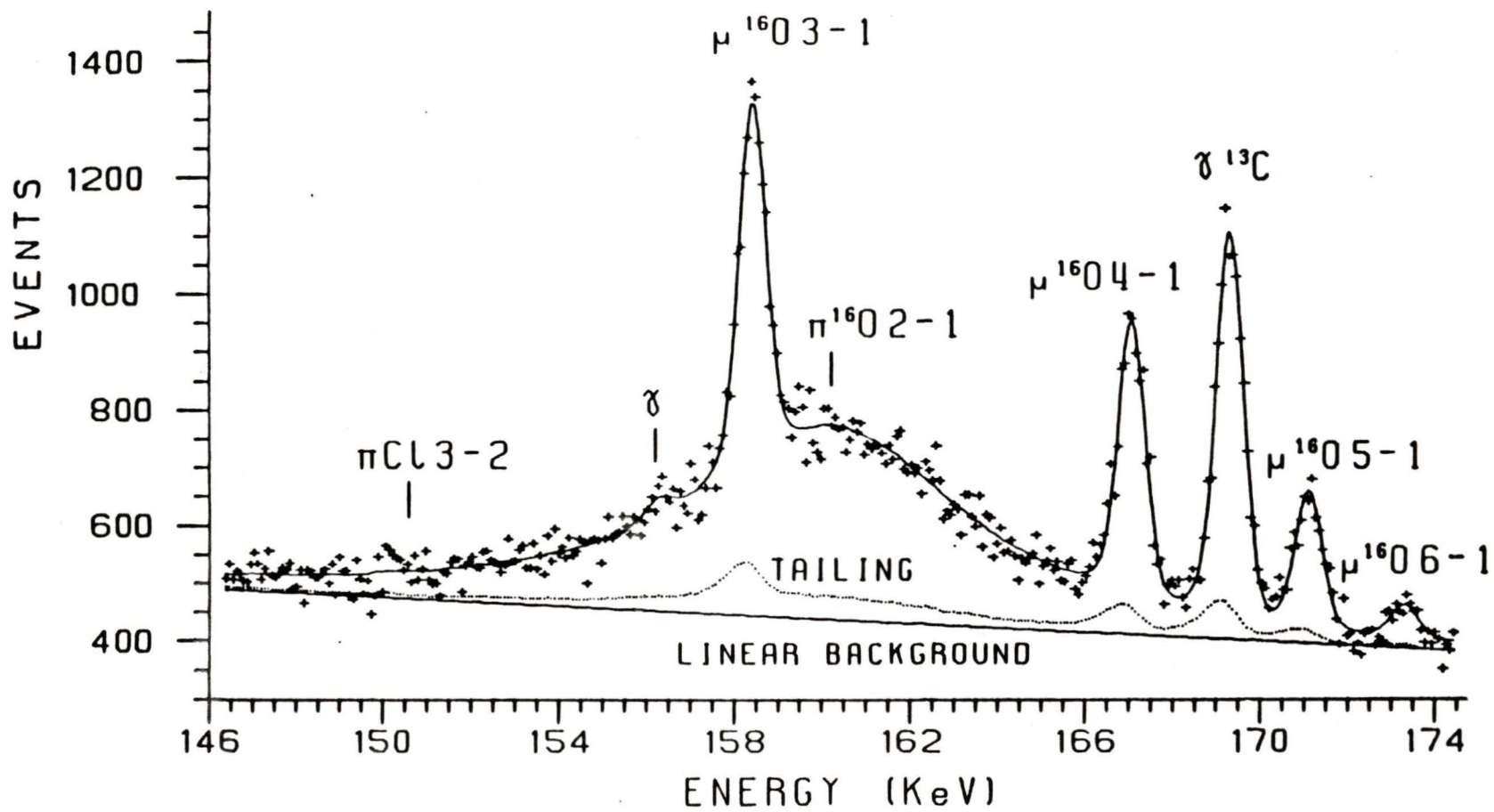


Figure 11. The $\pi^{160}\text{O}$ 2p-1s Fitting Window.

Table VIII

Peaks in the Fitting Window of the $\pi^{16}\text{O}$ 2p-1s X-ray

Peak	Energy (keV) (1)	Intensity (events)
$\pi^{18}\text{O}$ 2p-1s	155.701 fixed	111 fixed
$\gamma^{182}\text{Ta}$	156.298 (.006)	263 (113)
μO 3p-1s	158.448 (.012)	5173 (152)
$\pi^{16}\text{O}$ 2p-1s	160.286 (.074)	41583 (1727)
μO 4p-1s	167.081 (.012)	4020 (117)
$\gamma^{13}\text{C}$	169.315 (.006)	5632 (125)
μO 5p-1s	171.113 (.020)	1994 (105)
μO 6p-1s	173.347 (.073)	467 (96)

(1) Errors listed are statistical.

Table IX			
Measured Energies, Hadronic Shifts and Widths of the $\pi^{16,18}\text{O}$ 2p-1s X-rays			
	E (keV)	ϵ (keV)	Γ (keV)
$\pi^{18}\text{O}$ 2p-1s	155.792 (.160)	-19.63 (.20)	5.97 (.59)
$\pi^{16}\text{O}$ 2p-1s	160.286 (.090)	-15.13 (.13)	7.32 (.30)

Table X				
Contributions to the Uncertainties in the Measured Energies and Widths of the $\pi^{16,18}\text{O}$ 2p-1s X-rays				
	^{18}O		^{16}O	
	ΔE (eV)	$\Delta\Gamma$ (eV)	E (eV)	$\Delta\Gamma$ (eV)
Statistics	105	403	74	285
% ^{16}O Content	110	420	---	---
Detector Efficiency	6	5	5	0.2
Tailing	50	100	50	100
Calibration	11	0.2	12	0.2
Resolution	5	13	5	13
Totals	160	590	90	300

position of the $\pi\text{Cl } 3\text{d-}2\text{p}$ line is shown only for information; although this line appears in the $\pi^{18}\text{O}$ spectrum, its intensity in the fitted spectrum of $\pi^{16}\text{O}$ was not significant. This is probably because the ratio of pions stopping in the scintillator wrapping to pions stopping in the oxygen target is much smaller for the thicker ^{16}O target (2.0g/cm^2) than for the ^{18}O target (0.5g/cm^2). The intensity of the $\pi^{18}\text{O } 2\text{p-}1\text{s}$ line was fixed at 0.2%, the natural relative abundance of ^{18}O . The gamma ray from ^{182}Ta was due to accidental coincidences of source events with the target event gate (Section 3.7). Because two of the ^{182}Ta gamma rays, at 152 and 156 keV, would have appeared directly on the $\pi^{16,18}\text{O } 2\text{p-}1\text{s}$ peaks, ^{182}Ta was not used during the ^{18}O runs, and was used only for a short time during the ^{16}O runs. The intensity of the gamma ray from ^{13}C at 169 keV was smaller by about one third than its intensity in the $\pi^{18}\text{O}$ spectrum.

The results of the analysis are shown in Table VIII, and the various contributions to the uncertainties are shown in Table X.

4.8 Analysis of the $\pi^{16,18}\text{O } 3\text{d-}2\text{p}$ X-ray lines

There were two distinct goals in the analysis of the $\pi^{16,18}\text{O}$ 3d-2p X-ray lines. The first was measurement of the 3d-2p transition energies and linewidths. From the linewidths of both 3d-2p and 2p-1s transitions the 2p level width could have been obtained. The second was an analysis of the $\pi^{18}\text{O } 3\text{d-}2\text{p}$ line to obtain the relative intensity of the $\pi^{16}\text{O}$ component, as an independent measurement of the relative amount of ^{16}O present during data acquisition with the ^{18}O target.

However, even moderately good fits could not be made to either of these peaks. The best fits had very high χ^2 per degree of freedom (approximately 6.8 and 17.0 respectively for ^{16}O and ^{18}O), and the $\pi^{16}\text{O}$ component of the $\pi^{18}\text{O}$ peak could not be resolved. Attempts to include it in the $\pi^{18}\text{O}$ fits led to non-convergence with high negative areas for either the ^{16}O or the ^{18}O component, depending on other fit parameters. Both the $\pi^{18}\text{O}$ and the $\pi^{16}\text{O}$ 3d-2p peaks had very high statistics. Each peak had only three unidentified gamma rays of low intensity in its fitting window, and they were very well resolved by the fitting program. The prompt spectra in the fitting windows of the $\pi^{18}\text{O}$ and $\pi^{16}\text{O}$ 3d-2p peaks are shown in Figures 12 and 13.

It is possible that high statistics were the problem; the lineshape may have been so well-determined that it showed details which were not included in the fitting model, which had been developed from peaks with poorer statistics. High energy tailing, which did occur in both O 3d-2p peaks, would be one such detail of lineshape not included in the present fitting model. Imperfect pole-zero cancellation in the shaping amplifier before the ADC, resulting in overshoot of the ADC input pulses, would produce high energy tails on spectrum peaks.

The energies and linewidths obtained were:

$$\begin{array}{ll}
 ^{16}\text{O}: & E = 32.836 \pm 0.002 \text{ keV} \quad \Gamma = 63.5 \pm 3.2 \text{ eV} \\
 ^{18}\text{O}: & E = 32.821 \pm 0.003 \text{ keV} \quad \Gamma = 49.7 \pm 6.1 \text{ eV} .
 \end{array}$$

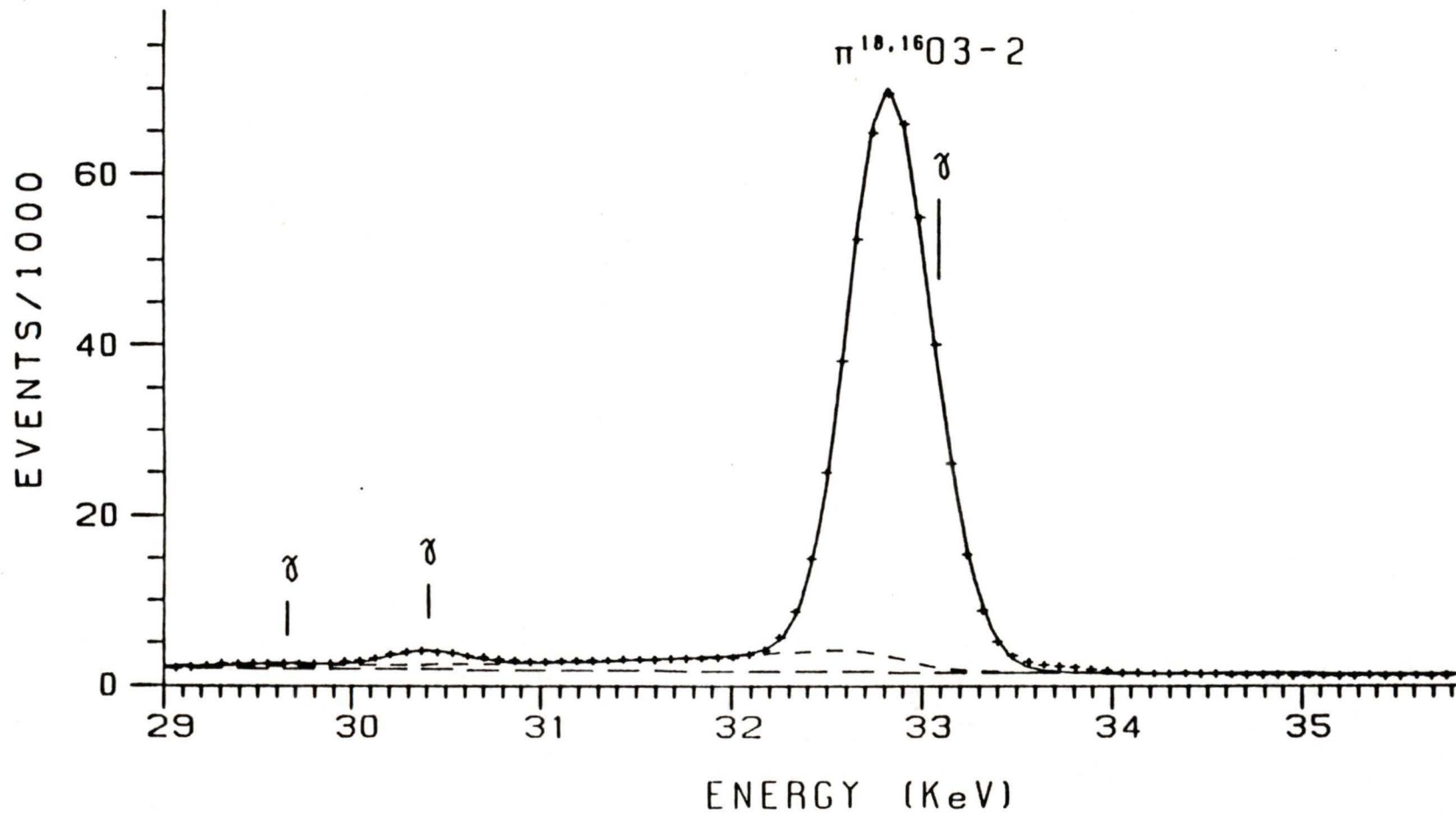


Figure 12. The $\pi^{18}\text{O}$ 3d-2p Fitting Window.

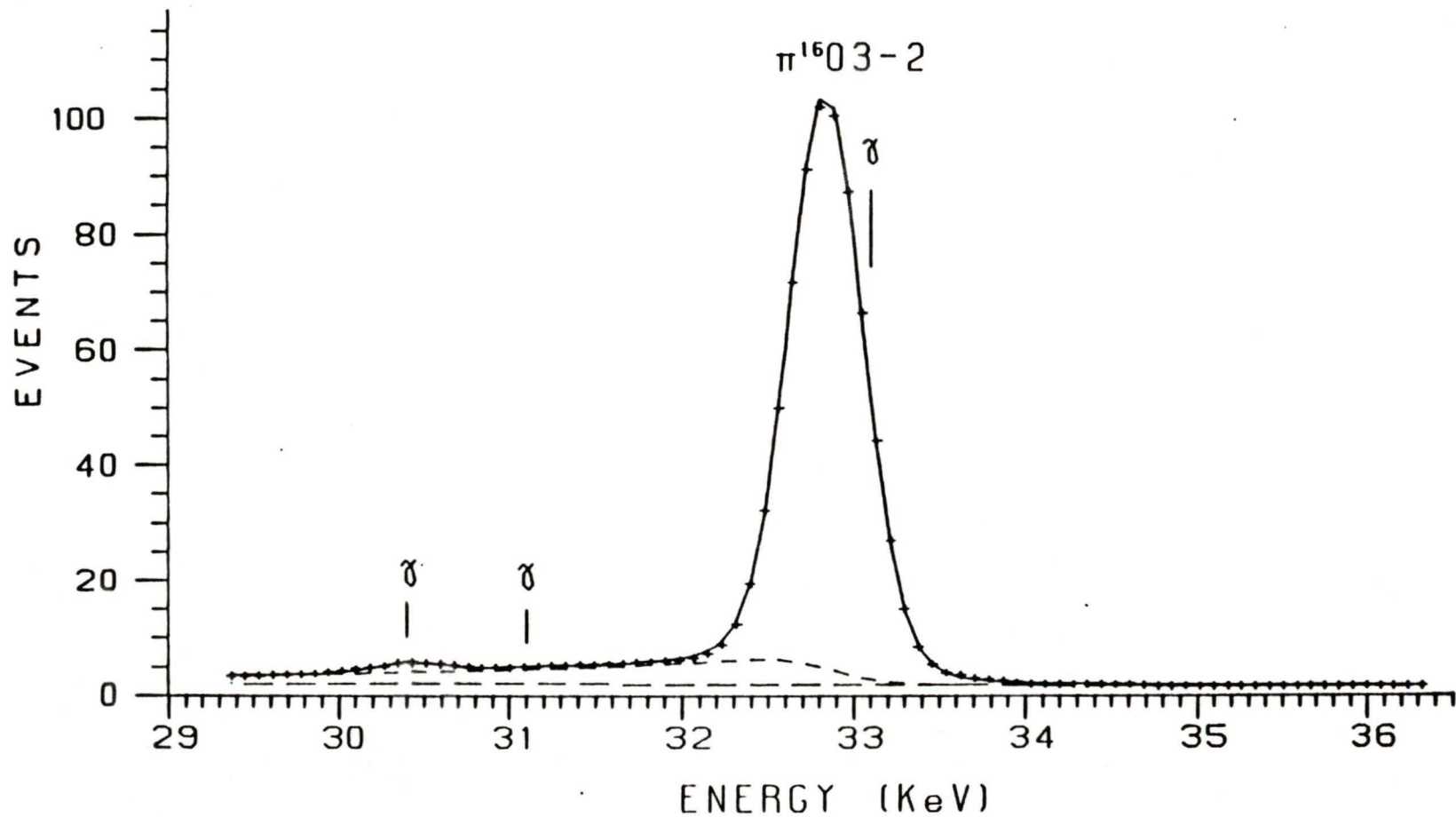


Figure 13. The $\pi^{16}O$ 3d-2p Fitting Window.

The errors are statistical only. By comparison, theoretical values are:

$$^{16}\text{O}: E = 32.856 \text{ keV} \quad \Gamma = 6.2 \text{ eV}$$

$$^{18}\text{O}: E = 32.890 \text{ keV} \quad \Gamma = 6.8 \text{ eV} .$$

The agreement with theoretical energies is not bad. However, the fitted widths are different from theory by about a factor of ten. This cannot be used as evidence for a significant ^{16}O component under the $\pi^{18}\text{O}$ peak, since it is true of both $\pi^{18}\text{O}$ and $\pi^{16}\text{O}$ 3d-2p peaks.

4.9 Analysis of the $\mu^{16}, ^{18}\text{O}$ X-ray lines

Although no data were taken with the beam tuned to stop muons, enough muons stopped in both targets to produce muonic oxygen peaks in the prompt spectra with sufficient intensity to measure the X-ray transition energies. The results are shown in Table XI. They are compared to a recent measurement of the muonic X-rays of oxygen (Backenstoss 1980).

The energies of the $\mu^{16}\text{O}$ and the $\mu^{18}\text{O}$ 2p-1s peaks are in agreement with the other recent results. There was some difficulty in fitting the two peaks, because each was located on a boundary between two timing cut regions. As discussed in Section 3.7, the energy range of target events was divided into 16 equal intervals, and separate timing cuts, sorting target events into prompt or delayed, were made for each energy interval. Since the intensity ratio of pion:muon events varied with the timing cut, small steps occurred in the background at boundaries between neighboring intervals whose timing cuts were

slightly different. The $\mu^{16}\text{O}$ and $\mu^{18}\text{O}$ 2p-1s peak centroids were each about 650 eV away from timing cut boundaries. The detector resolution at 133 keV is about 675 eV, so the low energy end of each peak actually was on the boundary. The muon intensity had at most a 5% drop at that point, while the relative pion intensity increased slightly, creating a step in the background. This resulted in large (>200%) errors in the fitted backgrounds, which were very sensitive to the location of the fitting window. The χ^2 per degree of freedom of each fit was, however, good ($\chi^2 \approx 1.0$) and the peak centroids varied by only 1 eV over wide choices of window.

The agreement of the $\mu^{18}\text{O}$ 3p-1s energies is good, while the $\mu^{16}\text{O}$ results are not in agreement. This may be due to the fact that the $\mu^{16}\text{O}$ peak lies near the center of the broad $\pi^{16}\text{O}$ 2p-1s peak, while the $\mu^{18}\text{O}$ peak lies well down the high energy side of the $\pi^{18}\text{O}$ peak, where the curve of the broad peak more closely approximates a straight line over the width of the muon peak.

The 4p-1s energies are in good agreement for both isotopes. The 5p-1s energies are in good agreement for $\mu^{16}\text{O}$, but differ by five standard deviations for $\mu^{18}\text{O}$. In the present experiment, the $\mu^{18}\text{O}$ 5p-1s peak is about 10% wider than other peaks in the fitting window, which is possible evidence for the presence of a ^{27}Al gamma ray under the $\mu^{18}\text{O}$ peak. The two peaks could not be resolved by the fitting program (the total intensity was only 800 events), so the $\mu^{18}\text{O}$ 5p-1s line was fitted as a single peak. The centroid, at 170.933 ± 0.036 keV,

was halfway between the ^{27}Al gamma ray energy of 170.70 ± 0.05 keV and the SIN results of 171.198 ± 0.050 keV.

Table XI

Comparison of Experimental Energies (in keV) of the $\mu^{16}\text{O}$ and
 $\mu^{18}\text{O}$ np-1s X-rays with Recent Experimental Results

	^{16}O	
	TRIUMF (1)	SIN (2)
2p-1s	133.536 (.009)	133.525 (.015)
3p-1s	158.448 (.015)	158.408 (.015)
4p-1s	167.081 (.015)	167.114 (.015)
5p-1s	171.113 (.022)	171.144 (.016)
	^{18}O	
	TRIUMF (1)	SIN (2)
2p-1s	133.535 (.009)	133.553 (.016)
3p-1s	158.422 (.025)	158.452 (.027)
4p-1s	167.148 (.047)	167.165 (.032)
5p-1s	170.933 (.036)	171.198 (.050)

CHAPTER 5DISCUSSION OF RESULTS AND CONCLUSIONS5.1 Theoretical predictions

The results are shown and compared to all other published experimental results and to theory in Table XII, and also in Figures 14 and 15. The optical model predictions were calculated using the code of Krell and Ericson (1969), which includes the effects of finite size and vacuum polarization. The strong interaction potential model (II) parameters of Poffenberger (1980) were used. These were obtained from a global fit to the most recent and most accurate pionic X-ray data for light nuclei, and are listed in Table XIII. Data from several nuclei with non-zero isospin were included in the fit for determination of the isovector terms; however, the only data available for isospin 1 nuclei were from ^{18}O . For both ^{16}O and ^{18}O , the results included in the global fit were obtained (Poffenberger 1980) by averaging, with weighting according to their respective errors, the present results and those of a recent experiment at SIN (Schwanner 1980). The optical potential parameters used in the present calculations are listed in Table XIII.

The harmonic oscillator charge and matter distribution radii used in calculating the theoretical energies and widths are shown in

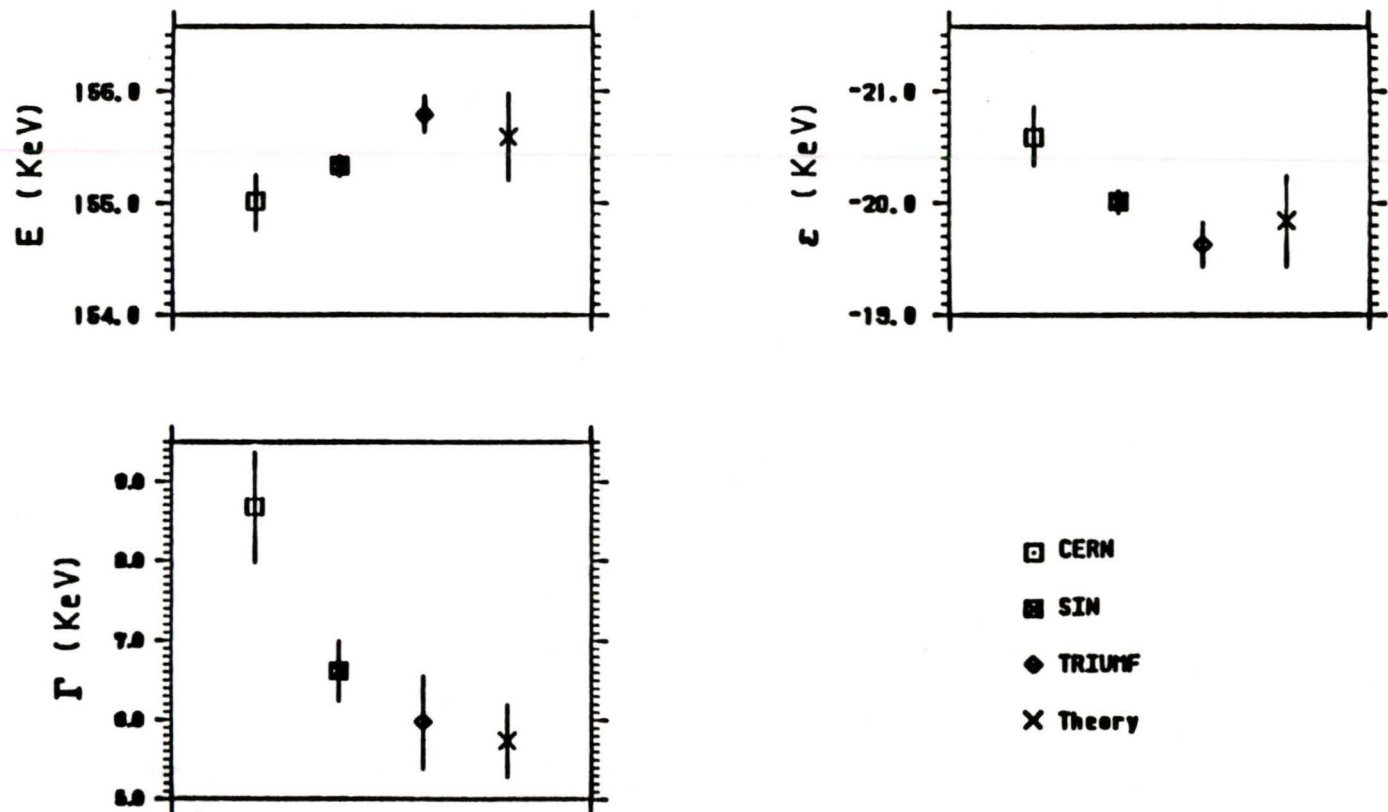


Figure 14. Comparison of the $\pi^{16}\text{O}$ 2p-1s X ray Energy, Hadronic Shift and Width with Other Experiments and Theory.

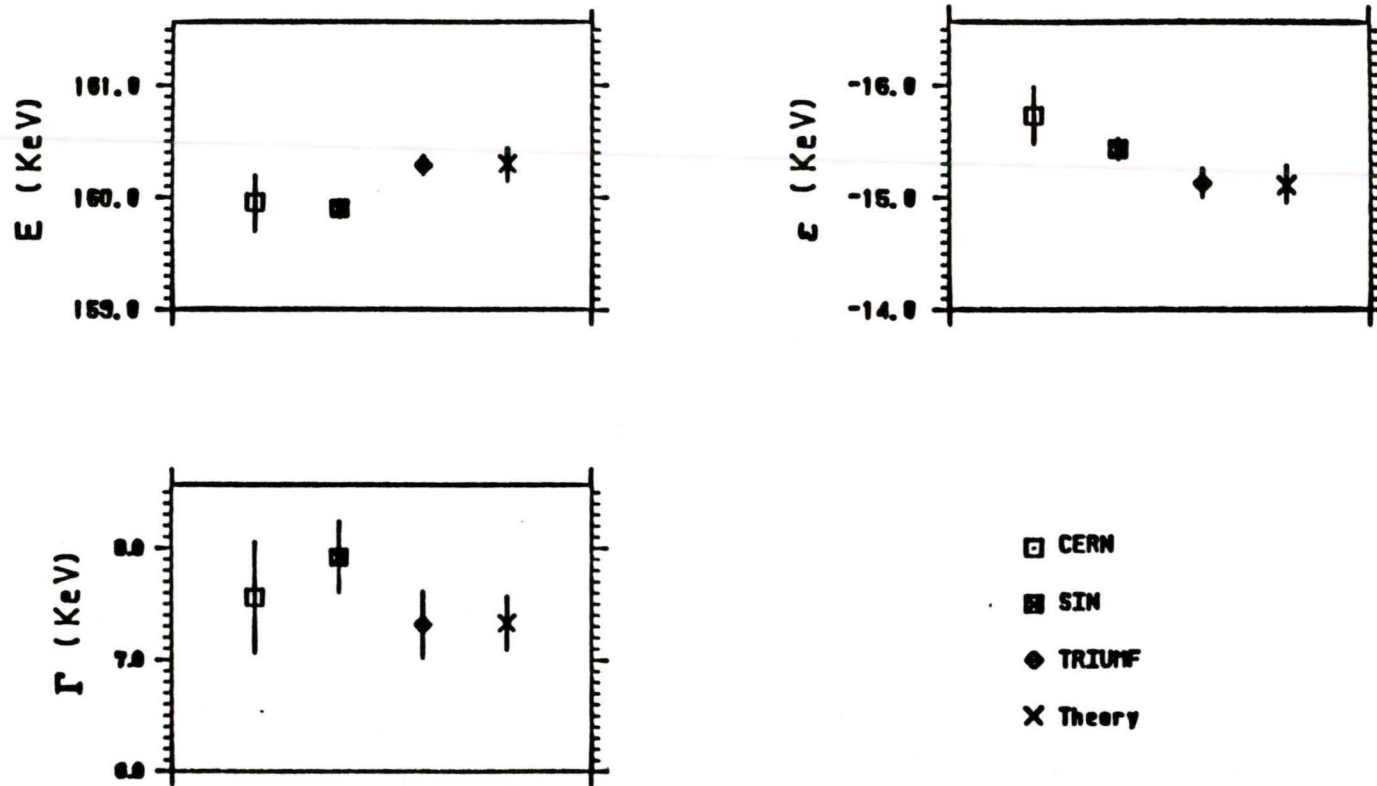


Figure 15. Comparison of the π^0 2p-1s X ray Energy, Hadronic Shift and Width with Other Experiments and Theory.

Table XII
 Comparison of the Measured Energies, Hadronic Shifts
 and Lorentzian Widths of the $\pi^{16,18}\text{O}$ 2p-1s X-rays
 with Other Experiments and Theory

	^{18}O		
	<u>E (keV)</u>	<u>ϵ (keV)</u>	<u>Γ (keV)</u>
TRIUMF (1)	155.792 (.160)	-19.63 (.20)	5.97 (.59)
SIN (2)	155.327 (.105)	-20.01 (.11)	6.62 (.38)
CERN (3)	155.01 (.25)	-20.59 (.26)	8.67 (.7)
Theory (4)	155.59 (.39)	-19.84 (.41)	5.73 (.46)
	^{16}O		
	<u>E (keV)</u>	<u>ϵ (keV)</u>	<u>Γ (keV)</u>
TRIUMF (1)	160.286 (.090)	-15.13 (.13)	7.32 (.30)
SIN (2)	159.900 (.090)	-15.43 (.10)	7.92 (.32)
CERN (3)	159.95 (.25)	-15.73 (.26)	7.56 (.50)
Theory (4)	160.293 (.15)	-15.12 (.17)	7.33 (.24)

- (1) Present experiment.
 (2) Schwanner et al. (1980).
 (3) Backenstoss et al. (1967).
 (4) Calculated with the optical model (II) of Poffenberger (1980).

Table XIII
Pion-nucleus Optical Potential Parameters Used in the
Present Analysis (1)

$b_0 (m_\pi^{-1})$	$b_1 (m_\pi^{-3})$	$c_0 (m_\pi^{-3})$	$c_1 (m_\pi^{-3})$
-0.0155	-0.0949	0.241	0.0
$\text{Re}B_0 (m_\pi^{-4})$	$\text{Im}B_0 (m_\pi^{-4})$	$\text{Im}C_0 (m_\pi^{-6})$	ξ
-0.0501	0.04545	0.112	1.00

(1) From the Model II of Poffenberger (1980).

Table XIV. The neutron radii were from recent π^- elastic scattering results (Johnson 1979), suitably corrected for the lower isotopic purity of the target discovered after the analysis of the scattering data. (The scattering target was made of the same H_2O^{18} gel used in the present experiment.) The error shown for $r_n(^{18}\text{O})$ is due to the uncertainty in isotopic purity of the target. The charge radii were from the recent measurements by electron elastic scattering of Miska et al. (1979). The proton radii were obtained by unfolding the proton and neutron charge and magnetic form factors (listed as total charge form factors in Table XIV). The errors shown in the theoretical π^0 2p-1s energies and linewidths were due to the uncertainties in the optical model and the charge distribution.

The strong interaction shifts, ϵ (keV), are defined by

$$\epsilon = E_{\text{exp}} - E_{\text{em}}$$

where the purely electromagnetic binding energy E_{em} includes the effects of finite size and vacuum polarization. The uncertainty in E_{em} is due principally to the uncertainty in the charge radius, and was added in quadrature with the uncertainty in E_{exp} to give the total uncertainty in ϵ .

Table XIV			
Charge and Matter Distributions Used in Theoretical Calculations of Energies and Linewidths (in fm)			
	$r_n(1)$	$r_p(2)$	Total Charge Form Factor (3)
^{16}O	2.59	2.610	0.766
^{18}O	2.79 ± 0.03	2.700 ± 0.005	0.718

- (1) Johnson et al. (1979), and B. Barnett, private communication.
 (2) Miska et al. (1979).
 (3) Poffenberger (1980).

5.2 Comparison of results with other experiments and theory

The agreement of present results with optical model predictions is excellent for all results with both isotopes (Table XII). The agreement with other measurements is not as good. The present ^{18}O width is in agreement with the SIN results, but not with the older CERN results. On the other hand, the present ^{16}O width is in agreement with the CERN results, but is two standard deviations away from the SIN results. Perhaps the most striking feature of a comparison of the values of the widths for both isotopes is the trend, seen in both

recent experiments and theory, to a smaller width for the $\pi^{18}\text{O}$ 2p-1s line than for the $\pi^{16}\text{O}$. In fact, the agreement of the present results with both SIN results and theory is excellent for the isotope shift as seen in Table XV. The smaller width for $\pi^{18}\text{O}$, a reversal of the early CERN results, can be explained by the dominance of the repulsive s-wave part of the potential in the 1s state, which causes the pion wavefunction to move further out when two neutrons are added to the closed shells of ^{16}O . The resulting smaller overlap of pion and nuclear wavefunctions lessens the probability of pion absorption, leading to the smaller observed (and predicted) width for $\pi^{18}\text{O}$.

The measured X-ray energies of the present experiment are higher by about 400 eV, for both isotopes, than the SIN results. The difference is nearly three standard deviations in the case of ^{18}O , and four standard deviations for the ^{16}O results. These apparently systematic differences cannot be due to a difference in energy calibrations, since the muon peak energies of both experiments, within the pionic 2p-1s fitting windows, are in agreement to 40 eV or less. The differences may be due to the use of a different lineshape model in the fitting programs, which could lead to differences of equal sign and nearly equal magnitude in fitted peak centroids for peaks of approximately the same shape and intensity, as the $\pi^{16,18}\text{O}$ 2p-1s lines.

The comparison in Table XII of the present X-ray energies and hadronic shifts with the SIN results shows an apparent discrepancy. For

^{18}O , the difference between the present and the SIN hadronic shifts is 380 eV, while the difference in X-ray energies is 465 eV, an apparent discrepancy of 85 eV. (For ^{16}O , the difference in measured hadronic shifts is 300 eV, for X-ray energies, 386 eV). Since the hadronic shift is just

$$\epsilon = E_{\text{Xray}} - E_{\text{em}},$$

where E_{em} is the calculated electromagnetic transition energy, the difference in hadronic shifts between the two measurements should be equal to the difference in X-ray energies, unless different values of E_{em} are used. In fact, the electromagnetic transition energies used in the SIN analysis (Schwanner 1980) were smaller by 88eV and 87eV, for ^{18}O and ^{16}O , respectively, than those used in the present analysis. The differences are probably due to the the use of different charge radii. In the SIN analysis, the charge radii were obtained from analysis of muon lines in the experimental spectra. In the present analysis, charge radii from recent electron elastic scattering results (Miska 1979) were used. They were larger by .006 mF and .008 mF (^{18}O and ^{16}O) than those used in the SIN analysis.

The isotope difference in the hadronic shifts, $\epsilon_{18} - \epsilon_{16}$, measured in the present experiment is in good agreement with the recent SIN results and with theory, as shown in Table XV; the agreement with the earlier CERN results is not as good.

Table XV
 Comparison of Isotope Effects with Other Experiments
 and with Theory

	Isotope Effects: $^{18}\text{O} - ^{16}\text{O}$	
	$\Delta\varepsilon$ (keV)	$\Delta\Gamma$ (keV)
TRIUMF (1)	-4.50 (.24)	-1.35 (.66)
SIN (2)	-4.58 (.14)	-1.30 (.50)
CERN (3)	-4.86 (.38)	1.01 (.86)
Theory (4)	-4.72 (.44)	-1.60 (.52)

- (1) Present experiment.
- (2) Schwanner et al. (1980).
- (3) Backenstoss et al. (1967).
- (4) From optical model (II) results of Poffenberger (1980).

5.3 Conclusions and recommendations

The special importance of pionic X-ray measurements on the isotope pair $^{16,18}\text{O}$, particularly of the $2p-1s$ line broadened by the strong interaction of the pion with the nucleus, is twofold. The isotope differences in the hadronic shifts and Lorentzian widths are measures of nuclear structure effects arising from the addition of two neutrons to the closed shells of ^{16}O . The isotope ^{18}O is one of only two stable light nuclei with $t=2$ for which the pionic $2p-1s$ X-ray may be readily observed (the other is ^{22}Ne (Olaniyi 1981)). The isotope difference in the $2p-1s$ hadronic shift, $\epsilon_{18} - \epsilon_{16}$, provides a more stringent test of the local isovector term, b_1 , in the pion-nucleus potential than isotope pairs with $t=0, t=1$. The non-local isovector term, c_1 , in the optical model used in this analysis, was zero. Isovector absorptive terms, B_1 and C_1 , were not included because no evidence was found for them in the global fit to recent pionic X-ray data for light nuclei (Poffenberger 1980).

Since the two most recent measurements of the hadronic $2p-1s$ shifts in $\pi^{16}\text{O}$ and $\pi^{18}\text{O}$ do not agree, although the isotope shifts are in agreement, it would be of interest to measure the $\pi^{16,18}\text{O}$ $2p-1s$ X-ray lines more accurately. Recommendations to help achieve this are: for ^{16}O , obtaining higher statistics (the principal contribution to the uncertainties in the present results); for ^{18}O , higher statistics and a more accurate determination of the amount of ^{16}O present (the two principal and nearly equal contributions to the

uncertainties in the present results). The latter could be achieved by: eliminating the oxygen in the air path between the defining counter, the veto (anti-coincidence) counter, and the detector, by inserting a bag of helium; by taking empty target runs to measure the amount of ^{16}O present outside the target material; and by doing a careful analysis, perhaps by mass spectroscopy, of the target material just prior to the experiment. The measurement of the pionic 3d-2p lines could be improved by more careful attention to adjustments such as pole-zero cancellation in the shaping amplifiers before the ADC, which affect lineshapes of very high intensity peaks. The measurement of muonic X-ray energies would be considerably improved by taking muon-tuned runs, especially in the case of the 3p-1s and higher lines, which appear in the broad π^0 2p-1s fitting window. The use of timing cuts which vary smoothly with energy would avoid the production of the steps in the background which made analysis of the $\mu^{16,18}\text{O}$ 2p-1s lines so difficult in the present experiment.

In conclusion then, to resolve the disagreements between the two recent pionic oxygen measurements, and with the recent measurement of pionic $^{20,22}\text{Ne}$ (Olaniyi 1981) providing another light isotope pair with $t=0$, $t=2$, it would be interesting and useful to measure more accurately the pionic 2p-1s transition in $^{16,18}\text{O}$.

REFERENCES

- N.M.M. Al-Qazzaz, G.A. Beer, G.R. Mason, A. Olin, R.M. Pearce, D.A. Bryman, J.A. Macdonald, J.-M. Poutissou, P.A. Reeve, M.D. Hasinoff, and T. Suzuki, The TRIUMF Stopped π - μ Channel, Nuclear Instruments and Methods, 174 (1980) 35.
- G. Backenstoss, Pionic Atoms, Annual Review of Nuclear Science, 20 (1970) 467.
- G. Backenstoss, S. Charalambus, H. Daniel, H. Koch, G. Poelz, H. Schmitt, and L. Tauscher, Pionic 2p-1s Transitions, Physics Letters, 25B (1967) 365.
- G. Backenstoss, W. Kowald, I. Schwanner, L. Tauscher, H.J. Weyer, D. Gotta, R. Guigas, Precision Determination of the Difference of the Charge Radii of ^{16}O and ^{18}O , Physics Letters, 95B (1980) 212.
- C.J. Batty, S.F. Biagi, E. Friedman, S.D. Hoath, J.D. Davies, G.J. Pyle, G.T.A. Squier, D.M. Asbury, and A. Guberman, Strong Interaction Effects in Pionic Atoms, Nuclear Physics, A322 (1979) 445.
- G.E. Brown, Proceedings of the Conference on Meson-Nuclear Physics, Pittsburgh, p.655 (1976).
- M. Ericson and T.E.O. Ericson, Optical Properties of Low Energy Pions in Nuclei, Annals of Physics, 36 (1966) 323.
- T.E.O. Ericson, The Pion-Nucleus Interaction, Proceedings of the Banff Summer School on Intermediate Energy Nuclear Physics,

- p. 102, eds. G.C. Neilson, W.C. Olsen, and S. Varma, University of Alberta, 1970.
- E. Friedman and A. Gal, Investigations of the Pion Nucleus Optical Potential from Pionic Atoms, to be published (1980).
- R.J. Gehrke, R.G. Helmer, and R.C. Greenwood, Precise Relative γ -ray Intensities for Calibration of Ge Semiconductor Detectors, Nuclear Instruments and Methods, 147 (1977) 405.
- F.S. Goulding and D.A. Landis, Semiconductor Detector Spectrometer Electronics, in Nuclear Spectroscopy and Reactions, Part A, ed. J. Cerny, Academic Press, New York, 1974.
- F.S. Goulding and R.H. Pehl, Semiconductor Radiation Detectors in Nuclear Spectroscopy and Reactions, ed. J. Cerny, Academic Press, New York, 1974.
- R.G. Helmer, R.C. Greenwood, and R.J. Gehrke, Reevaluation of Precise γ -ray Energies for Calibration of Ge(Li) Spectrometers, Nuclear Instruments and Methods, 155 (1978) 189.
- J. Hufner, Pions Interact with Nuclei, Physics Reports, 21 (1975) 1.
- R.R. Johnson, T. Masterson, B. Bassalleck, W. Gyles, T. Marks, K.L. Erdman, A.W. Thomas, D.R. Gill, E. Rost, J.J. Kraushaar, J. Alster, C. Sabev, J. Arvieux, and M. Krell, Neutron Radii Determinations from the Ratio of π^- Elastic Scattering from $^{12,13}\text{C}$ and $^{16,18}\text{O}$, Physical Review Letters, 43 (1979) 844.
- M. Krell, The Pionic (Kaonic) Atom Program: PIATOM, University of Victoria, TRIUMF Report VPN-77-5, 1977.

- M. Krell and T.E.O. Ericson, Energy Levels and Wavefunctions of Pionic Atoms, Nuclear Physics, B11 (1969) 521.
- D.F. Measday, M.R. Menard, and J.E. Spuller, TRIUMF Kinematics Handbook, TRIUMF, University of British Columbia (1975).
- H. Miska, B. Norum, M.V. Hynes, W. Bertozzi, S. Kowalski, F.N. Rad, C.P. Sargent, T. Sasanuma, and B.L. Berman, Precise Measurement of the Charge Distribution Differences of the Oxygen Isotopes, Physics Letters, 83B (1979) 165.
- M.M. Nagels, T.A. Rijken, J.J. deSwart, G.C. Oades, J.L. Petersen, A.C. Irving, C. Jarlskog, W. Pfeil, H. Pilkuhn, and H.P. Jakob, Compilation of Coupling Constants and Low-Energy Parameters, Nuclear Physics, B147 (1979) 189.
- B.H. Olaniyi, G.A. Beer, A. Fry, J.A. Macdonald, G.R. Mason, A. Olin, and R.M. Pearce, Pionic K_{α} X-ray Energy and Linewidth in ^{20}Ne and ^{22}Ne , TRIUMF Preprint TRI-PP-81-43 (1981).
- A. Olin, JAGSPOT, A Code for Fitting Complex Gamma Ray Spectra, University of Victoria, TRIUMF Report VPN-78-2, 1978.
- Particle Data Group, Particle Properties Data Booklet, Lawrence Berkeley Laboratory, University of California, 1978.
- P.R. Poffenberger, Ph.D. Thesis, University of Victoria (1980).
- H. Poth, Physik Daten, Compilation of Data from Hadronic Atoms, Institut fur Experimentelle Kernphysik der Universitat Karlsruhe, Germany, 1979.
- R.J. Powers, K.-C. Wang, M.V. Hoehn, E.B. Shera, H.D. Wohlfahrt,

- and A.R. Kunselman, Experimental Study of Pionic Ca and Ti and Examination of the Pion-Nucleus Potential for Low-Z Nuclei, Nuclear Physics, A336 (1980) 475.
- F. Scheck, Interactions of Pions with Nuclei, in Nuclear and Particle Physics at Intermediate Energies, ed. J.B. Warren, Plenum Press (1975).
- I. Schwanner, R. Abela, G. Backenstoss, W. Kowald, P. Pavlopoulos, L. Tauscher, H.J. Weyer, P. Blum, M. Dorr, W. Fetscher, D. Gotta, R. Guigas, H. Koch, H. Poth, G.Schmidt, and H. Ullrich, Isotope Effects in Light Pionic Atoms, Physics Letters, 96B (1980) 268.
- L. Tauscher and W. Schneider, Optical Potential Calculations for the $1s$ Level in Pionic Atoms, Zeitschrift fur Physik, 271 (1974) 409.
- W.S.C. Williams, An Introduction to Elementary Particles, Academic Press, New York, 1971.

APPENDIX APARTIAL WAVE ANALYSIS OF PION-NUCLEON SCATTERING

Following the development of Williams (1971), both incoming and outgoing pion waves in a pion-nucleon scattering event may be expanded in partial waves which are eigenfunctions of both ℓ^2 and ℓ_z . When the scattering is elastic, the only effect of the scattering potential is to change the phase of the scattered wave with respect to the incoming wave, by an amount δ_ℓ , which is called the phase shift. The scattering amplitude may then be expanded in partial waves to give

$$f(E, \Theta) = \sum_{\ell=0}^{\infty} \frac{e^{2i\delta_\ell} - 1}{2ik} (2\ell+1) P_\ell(\cos \Theta) \quad (\text{A.1})$$

where the phase shifts δ_ℓ depend on the energy, E, of the incoming particle. When $\delta_\ell \ll 1$,

$$\begin{aligned} e^{2i\delta_\ell} - 1 &\cong (1 + 2i\delta_\ell) - 1 \\ &\cong 2i\delta_\ell \end{aligned} \quad (\text{A.2})$$

and then (A.1) can be written as

$$f(E, \Theta) \cong \sum_{\ell=0}^{\infty} \frac{2i\delta_\ell}{2ik} (2\ell+1) P_\ell(\cos \Theta) . \quad (\text{A.3})$$

The generalized scattering length, a_ℓ , which actually has dimensions (length)^{2 ℓ +1}, is defined as

$$\lim_{k \rightarrow 0} \frac{\delta_\ell}{k^{2\ell+1}} = a_\ell . \quad (\text{A.4})$$

Then, in the limit of zero incident pion energy, which certainly holds for pionic atoms, the scattering amplitude may be written as

$$f(E=0, \Theta) = f(\Theta) \cong \sum_{\ell=0}^{\infty} a_{\ell} k^{2\ell} (2\ell+1) P_{\ell}(\cos \Theta) . \quad (\text{A.5})$$

Now taking into account the spin of the nucleon, which is a fermion, the wavefunctions must be multiplied by the spin function,

$$\chi\left(\frac{1}{2}, \pm\frac{1}{2}\right) .$$

Also, $P_{\ell}(\cos \Theta)$ may be replaced by the spherical harmonic

$$Y_{\ell}(\cos \Theta) = Y(\ell, \ell_z=0) ,$$

where

$$Y(\ell, 0) = \left(\frac{2\ell+1}{4\pi}\right)^{\frac{1}{2}} P_{\ell}(\cos \Theta) , \quad (\text{A.6})$$

so that, in (A.1),

$$P_{\ell}(\cos \Theta) \rightarrow \left(\frac{4\pi}{2\ell+1}\right)^{\frac{1}{2}} Y(\ell, 0) \chi\left(\frac{1}{2}, \pm\frac{1}{2}\right) . \quad (\text{A.7})$$

The total angular momentum of the $|\pi N\rangle$ system is either $j = \ell + \frac{1}{2}$ or

$j = \ell - \frac{1}{2}$; then (A.7) may be decomposed into eigenfunctions of total

angular momentum, $\phi_{\ell}(j, j_z)$, using vector addition of angular momentum:

$$\begin{aligned} Y(\ell, 0) \chi\left(\frac{1}{2}, \pm\frac{1}{2}\right) &= \langle \ell + \frac{1}{2}, \pm\frac{1}{2} | \ell 0 \frac{1}{2} \pm\frac{1}{2} \rangle \phi_{\ell}\left(\ell + \frac{1}{2}, \pm\frac{1}{2}\right) \\ &\quad + \langle \ell - \frac{1}{2}, \pm\frac{1}{2} | \ell 0 \frac{1}{2} \pm\frac{1}{2} \rangle \phi_{\ell}\left(\ell - \frac{1}{2}, \pm\frac{1}{2}\right) \\ &= \left(\frac{\ell+1}{2\ell+1}\right)^{\frac{1}{2}} \phi_{\ell}\left(\ell + \frac{1}{2}, \pm\frac{1}{2}\right) \mp \left(\frac{\ell}{2\ell+1}\right)^{\frac{1}{2}} \phi_{\ell}\left(\ell - \frac{1}{2}, \pm\frac{1}{2}\right) . \end{aligned} \quad (\text{A.8})$$

Since j is conserved, and scattering may be different in different j -states, a separate phase shift must be defined for each j -state:

$\delta_{\ell+}$, for $j = \ell + \frac{1}{2}$; $\delta_{\ell-}$, for $j = \ell - \frac{1}{2}$. Making this change, and using (A.7) and (A.8), the scattering amplitude (A.1) becomes

$$f(\Theta) = \sqrt{4\pi} \sum_{\ell=0}^{\infty} \left\{ f_{\ell+} \left(\ell + \frac{1}{2} \right)^{\frac{1}{2}} \phi_{\ell} \left(\ell + \frac{1}{2}, \pm \frac{1}{2} \right) \mp f_{\ell-} \left(\ell - \frac{1}{2} \right)^{\frac{1}{2}} \phi_{\ell} \left(\ell - \frac{1}{2}, \pm \frac{1}{2} \right) \right\}, \quad (\text{A.9})$$

where

$$f_{\ell\pm} = \frac{e^{2i\delta_{\ell\pm}} - 1}{2i}.$$

The energy dependence of the right-hand side of (A.9) is in the $f_{\ell\pm}$, which are called the partial wave amplitudes, for the scattering of the ℓ^{th} partial wave in the appropriate j -state.

During the scattering event, it is possible for the spin orientation of the nucleon to change, i.e., $\Delta s_z = \pm 1$. But j_z is conserved ($\Delta j_z = 0$), so that the outgoing wave must have $\Delta \ell_z = \pm 1$; this means the scattering amplitude must include terms in $Y(\ell, \ell_z \pm 1)$. This may be done using angular momentum decomposition of $\phi_{\ell}(j, j_z)$,

$$\begin{aligned} \phi_{\ell} \left(\ell + \frac{1}{2}, \pm \frac{1}{2} \right) &= \left(\frac{\ell + 1}{2\ell + 1} \right)^{\frac{1}{2}} Y(\ell, 0) \chi \left(\frac{1}{2}, \pm \frac{1}{2} \right) \\ &\quad + \left(\frac{\ell}{2\ell + 1} \right)^{\frac{1}{2}} Y(\ell, \pm 1) \chi \left(\frac{1}{2}, \mp \frac{1}{2} \right), \\ \phi_{\ell} \left(\ell - \frac{1}{2}, \pm \frac{1}{2} \right) &= \mp \left(\frac{\ell}{2\ell + 1} \right)^{\frac{1}{2}} Y(\ell, 0) \chi \left(\frac{1}{2}, \pm \frac{1}{2} \right) \\ &\quad \pm \left(\frac{\ell + 1}{2\ell + 1} \right)^{\frac{1}{2}} Y(\ell, \pm 1) \chi \left(\frac{1}{2}, \mp \frac{1}{2} \right), \end{aligned} \quad (\text{A.10})$$

in (A.9) to give

$$\begin{aligned}
f(\Theta) &= \left(\frac{4\pi}{2l+1}\right)^{\frac{1}{2}} \sum_{l=0}^{\infty} \left\{ [(l+1)f_{l^+} + lf_{l^-}] Y(l,0) \chi\left(\frac{1}{2}, \frac{1}{2}\right) \right. \\
&\quad \left. + [l(l+1)]^{\frac{1}{2}} (f_{l^+} - f_{l^-}) Y(l, \pm 1) \chi\left(\frac{1}{2}, \frac{1}{2}\right) \right\} \\
&= \sum_{l=0}^{\infty} \left\{ [(l+1)f_{l^+} + lf_{l^-}] P_l(\cos \Theta) \chi\left(\frac{1}{2}, \frac{1}{2}\right) \right. \\
&\quad \left. + (f_{l^+} - f_{l^-}) P_l^1(\cos \Theta) e^{\pm i\phi} \chi\left(\frac{1}{2}, \frac{1}{2}\right) \right\}.
\end{aligned} \tag{A.11}$$

The first term is the spin-nonflip amplitude, and since the incoming and outgoing spin states are identical, the spin function $\chi\left(\frac{1}{2}, \frac{1}{2}\right)$ may be dropped in the expansion for the scattering amplitude. The second term is the spin-flip amplitude, which may be simplified using an alternative way of writing the spin wavefunction, as follows.

First, take \mathbf{n} to be the unit vector normal to the plane of scattering,

$$\begin{aligned}
\mathbf{n} &= \frac{\vec{k}_i \times \vec{k}_f}{|\vec{k}_i \times \vec{k}_f|} \\
&= -i \sin \phi + j \cos \phi,
\end{aligned} \tag{A.12}$$

where ϕ is the azimuthal angle of the scattering plane. Then

$$\begin{aligned}
i\sigma \cdot \mathbf{n} &= i \cos \phi \begin{bmatrix} 0 & -i \\ +i & 0 \end{bmatrix} - i \sin \phi \begin{bmatrix} 0 & 1 \\ 1 & 0 \end{bmatrix} \\
&= \begin{bmatrix} 0 & e^{-i\phi} \\ -e^{+i\phi} & 0 \end{bmatrix},
\end{aligned} \tag{A.13}$$

where the σ_{xyz} are the Pauli spin matrices. In this representation of $\vec{\sigma}$,

$$\chi\left(\frac{1}{2}, \frac{1}{2}\right) = \begin{bmatrix} 1 \\ 0 \end{bmatrix}, \quad \text{and} \quad \chi\left(\frac{1}{2}, -\frac{1}{2}\right) = \begin{bmatrix} 0 \\ 1 \end{bmatrix}. \tag{A.14}$$

Then, operating with $-i\vec{\sigma} \cdot \mathbf{n}$ on the incoming spinors $\chi\left(\frac{1}{2}, \frac{1}{2}\right)$,

$$\begin{aligned}
 -i\sigma \cdot n \chi\left(\frac{1}{2}, +\frac{1}{2}\right) &= +e^{i\phi} \chi\left(\frac{1}{2}, -\frac{1}{2}\right) \\
 -i\sigma \cdot n \chi\left(\frac{1}{2}, -\frac{1}{2}\right) &= -e^{-i\phi} \chi\left(\frac{1}{2}, +\frac{1}{2}\right) .
 \end{aligned}
 \tag{A.15}$$

Comparing this with (A.11), it can be seen that the results are just the outgoing scattered spinors. Therefore the spin-flip terms in the scattering amplitude may be written using $-i\vec{\sigma} \cdot n$ in place of $\pm e^{\pm i\phi} \chi\left(\frac{1}{2}, \mp\frac{1}{2}\right)$, so that (A.11) becomes

$$\begin{aligned}
 f(\Theta) &= \sum_{\ell=0}^{\infty} \{ [(\ell+1) f_{\ell^+} + \ell f_{\ell^-}] P_{\ell}(\cos \Theta) \} \\
 &- i\vec{\sigma} \cdot \frac{\vec{k}_i \times \vec{k}_f}{|\vec{k}_i \times \vec{k}_f|} \sum_{\ell=0}^{\infty} [(f_{\ell^-} - f_{\ell^+}) P_{\ell}^1(\cos \Theta)] .
 \end{aligned}
 \tag{A.16}$$

APPENDIX BCALCULATION OF DEGRADER THICKNESS NECESSARY TO STOPPIONS IN THE OXYGEN TARGETS

The degrader material used was a set of 18 nickel-plated bars of beryllium stacked together to give a total thickness of 2.3g/cm^2 Be. Beryllium was chosen because the X-rays from pions stopping in it are well below the energy range of interest in this experiment, 140-180 keV. Pionic and muonic nickel X-rays are well above this energy range.

The incoming pion energy was 30 MeV. From the TRIUMF Kinematics Handbook (1975), the range of 30 MeV pions in the materials present in the path of the stopping pions is

$$\begin{aligned} \text{in Be: } & 4.7 \text{ g/cm}^2 \\ \text{C : } & 4.4 \text{ g/cm}^2 \\ \text{H}_2\text{O : } & 3.8 \text{ g/cm}^2 . \end{aligned}$$

The total thickness of material upstream of and including the stopping target was

$$\begin{aligned} \text{scintillators (3mm + 6mm + 3mm = 12mm) : } & 1.2 \text{ g/cm}^2 \text{ C} \\ \text{degrader : } & 2.3 \text{ g/cm}^2 \text{ Be} \\ \text{H}_2^{18}\text{O target, } & \frac{.5\text{g/cm}^2 \text{ H}_2\text{O}}{\sin 45} : .7 \text{ g/cm}^2 \text{ H}_2\text{O} \end{aligned}$$

giving an effective stopping power of each material, defined by thickness (g/cm^2)/ 30 MeV pion range (g/cm^2), of

scintillators : .30

degrader : .49

H_2^{18}O target : .18

Total : .97

where an effective stopping power of 1.0 brings 30 MeV pions to rest.

This approximate calculation of the stopping material required was quite adequate since the channel tune was varied slightly to optimize the pion stopping rate in the target. The H_2^{16}O target was $2 \text{ g}/\text{cm}^2$ thick, making the total thickness $6.4 \text{ g}/\text{cm}^2$, so the channel tune was reset each time the target was changed.

VITA

Surname: SAYRE Given Names: CHRISTINE IRENE

Place of Birth: LUBECK, GERMANY Date of Birth: July 13, 1948

Educational Institutions Attended, with Dates of Entering and Leaving:

UNIVERSITY OF TORONTO, TORONTO 1973 to 1976

UNIVERSITY OF VICTORIA, VICTORIA 1976 to 1983

_____ to _____

Degrees, Diplomas, Etc., Awarded, with Dates and Names of Institutions:

B.Sc. 1977 University of Toronto, Toronto

Honours and Awards:

University of Victoria Supplementary Graduate Study Scholarship,

1978-1980

Publications:

C.A. Fry, G.A. Beer, G.R. Mason, R.M. Pearce, P.R. Poffenberger,

C.I. Sayre, A. Olin, and J.A. Macdonald, Pionic X-rays from ¹², ¹³C,

Nuclear Physics A375 (1982) 325.

B. Evans, R. Harrop, D. Heywood, J. Mackintosh, R.W. Moore,
B.D. Pate, J.G. Rogers, T.J. Ruth, C. Sayre, H. Sprenger,
N. Van Oers, and Yao Xiao Guang, Engineering Developments on the
UBC-TRIUMF Modified PETT VI Positron Emission Tomograph,
IEEE Transactions on Nuclear Science, NS-30 (707), February, 1983.

PARTIAL COPYRIGHT LICENSE


I hereby grant the right to lend my thesis (the title of which is shown below) to users of the University of Victoria Library, and to make single copies only for such users or in response to a request from the library of any other university, or similar institution, on its behalf or for one of its users. I further agree that permission for extensive copying of this thesis for scholarly purposes may be granted by me or a member of the University designated by me. It is understood that copying or publication of this thesis for financial gain shall not be allowed without my written permission.

Title of Thesis

Pionic ^{16}O - ^{18}O Isotope Effects

Author



Signature 

Christine I. Sayre

Name

August 14, 1983

Date